All-Ceramic Li Batteries Based on Garnet Structured $Li_7La_3Zr_2O_{12}$

Chih-Long Tsai[a,*], Shicheng Yu[a], Hermann Tempel[a], Hans Kungl[a], Rüdiger-A. Eichel[a-c]

[a]Institut für Energie- und Klimaforschung (IEK-9: Grundlagen der Elektrochemie), Forschungszentrum Jülich, D-52425 Jülich, Germany

[b]Institut für Materialien und Prozesse für elektrochemische Energiespeicher– und wandler, RWTH Aachen University, D-52074 Aachen, Germany

[c]Institut für Energie- und Klimaforschung (IEK-12: Helmholtz-Institute Münster, Ionics in Energy Storage), Forschungszentrum Jülich, D-48149 Münster, Germany

Abstract

All-ceramic Li batteries (CLBs) are expected as next-generation energy storage devices because of their potential to have higher energy density and safety than nowadays Li-ion batteries. Garnet structured $Li_7La_3Zr_2O_{12}$ (LLZO) plays an important role on CLB developments due to its fast Li-ion conductivity, intrinsic stability towards Li and high chemical and electrochemical stabilities. After a decade of researches, many problems have been answered for LLZO-based CLB developments but still numerous challenges left to be solved. This review presents the latest efforts on the development of LLZO-based CLBs, which covers the advances in LLZO crystal structure to increase its ionic conductivity and progresses in the use of Li as the electrode, regarding to its intrinsic chemical stability towards Li and interface elaboration for allowing Li dendrite suppression. On the positive electrode developments, chemical compatibility of various active materials and strategies to circumvent the incompatibility issue at high sintering temperatures are inspected.

---

*Corresponding author: Chih-Long Tsai
Email: c.tsai@fz-juelich.de

1. Introduction

Since the first commercialization in 1991 by Sony, Li-ion batteries (LIBs) have been developed into one of the most popular energy storage device due to their high volumetric and gravimetric energy densities. The application of LIBs for nowadays covers from portable electronic devices, such as smart phones and laptops, to large-scale applications, such as electric vehicles and stationary energy storage for renewable energy sources. Nevertheless, the demand for a battery with even higher energy and power densities is stronger than ever because of the desire for extending working hours for a device between two charges of the used battery. All-ceramic Li batteries (CLBs) have been proposed to be one of the most promising technologies for next generation electrochemical energy storage regarding their high energy density by replacing graphite electrode to metallic Li electrode, extended cycle life because of no accumulated formation of solid electrolyte interface and inherent safety due to the non-flammable ceramic components.[1-2]

One of the key components for a CLB development is having a suitable solid state ionic conductor as its solid electrolyte. Among various Li-ion conductors, garnet structured materials based on $Li_7La_3Zr_2O_{12}$ (LLZO) has been attracting tremendous attention since the first report by Murugan *et al.* in 2007, due to its high Li-ionic conductivity (> 10^{-4} S cm^{-1} at RT), wide electrochemical window, stability against metallic Li, high ionic transference number (~1) and environment friendliness.[3] However, after more than a decade of intensive development, a demonstration of a practical CLB based on LLZO at/near RT, with area capacity > 3 mA h cm^{-2}, is still not available. Challenges regarding to CLB developments based on LLZO are linked to its Li dendrite formation, interface instability and high processing temperature that causes chemical instability between the used active electrode material and LLZO and internally elemental diffusion at high temperatures.

In this review, we mainly focus on reviewing the progress of CLB development by using garnet structured LLZO. Therefore, articles that apply organic polymer or liquid electrolytes in the electrochemical performances are excluded from this review. The review starts from the discussion of the ionic conductivity of LLZO by using different substitutions and their chemical stabilities toward metallic Li. It is then followed by the development of negative electrode by using metallic Li that causes interface instability and dendrite formation to short circuiting symmetric Li/LLZO/Li cells. It further covers the chemical compatibilities between LLZOs and active positive electrode materials at high sintering temperatures and strategies that are proposed to circumvent the chemical instability between LLZO and the used positive active electrode materials at high sintering temperatures so that the proof of concept CLBs can be demonstrated.

2. The Developments of $Li_7La_3Zr_2O_{12}$ Solid Electrolytes

2.1 The increases of Li-ion conductivities

The first highly conductive garnet structured LLZO was reported by Murugan et al. in 2007.[3] It was found at later time that there are two crystallographic modifications existing for LLZO; a cubic and a tetragonal phase. Due to the full occupation of Li-sites by Li-ions, tetragonal LLZO shows a complete ordering of the Li-ions and long Li-Li hopping distances while that for cubic LLZO only has partial occupation by Li-ions on the Li(1) and Li(2) sites to give short Li-Li hopping distances.[4] Therefore, the formation of tetragonal phase LLZO reduces its Li-ion conductivity from a cubic phase ones, $>10^{-4}$ $S{\cdot}cm^{-1}$, to a much lower value of $1x10^{-6}$ $S{\cdot}cm^{-1}$ at RT.[4-5] It is understood that the material was usually contaminated by Al during their high temperature sintering processes due to the reaction with frequently used alumina crucibles. Further researches on Al-substituted $Li_7La_3Zr_2O_{12}$ by using XRD, neutron powder diffraction, and TEM precession electron diffraction reveal that Al^{3+} is incorporated in the garnet lattices on the tetrahedral *24d* Li(1) sites, thus stabilizing the LLZO to cubic phase and resulting in the very short Li-Li distance in the migration pathway to give the good Li-ion-conduction properties when compared to the tetragonal one, **Figure 1(a, b).**[4, 6-8] Bernstein *et al.* used density functional theory and variable cell shape molecular dynamics simulations to investigate the driving force for the phase transition from tetragonal to cubic and suggested that the critical substitution concentration of Al^{3+} necessary to obtain highly conductive cubic phase of LLZO is at 0.2 ^{mol}%, i.e., $Li_{6.4}Al_{0.2}La_3Zr_2O_{12}$.[9] Later, Rangasamy *et al.* experimentally show that 0.204 ^{mol}% of Al^{3+} is required to stabilize LLZO as cubic phase at RT while 0.389 ^{mol}% of Al^{3+} is the limitation of Al^{3+} solubility in LLZO.[10] A phase transition from cubic to tetragonal LLZO was identified when the Li-ion content increased from 6.24 to 7.32 ^{mol}% due to the filling of Li(2) vacancies by the addition Li-ions, which distorts the structure from cubic to tetragonal phase for further uptake of Li in the garnet structure was also shown, **Figure 1(c)**. Since the incorporation of Al^{3+} from Al_2O_3 crucible to LLZO could dramatically affect the finally reported conductivity, a note on the used crucible for the sintering process of LLZO is always important for the evaluation on how a substitution could affect the final total conductivity of a LLZO sample, **Table 1**.

Xu *et al.* investigated the Li-ion transport mechanism in cubic phase $Li_{3+x}La_3M_2O_{12}$ (M = Te^{6+}, Nb^{5+}, Zr^{4+}) by using ab initio tools.[11] As the materials $Li_3La_3Te_2O_{12}$, $Li_5La_3Nb_2O_{12}$ and $Li_7La_3Zr_2$O12 are compared, the Li concentrations are not the only variables but also the valences of the dopants, i.e. Te^{6+}, Nb^{5+}, Zr^{4+}. They suggest that the conductivity is affected far more by Li-ion concentration than by different dopant elements or lattice parameters for LLZO, **Figure 1 (d).** When the Li-ion concentration is low, such as that in $Li_3LaTe_2O_{12}$, Li-ions only occupy tetrahedral Li(1) sites and not octahedral Li(2) sites. The Li(1) sites act as energetic traps to immobilize the Li-ions in these positions, leading to a low Li-ion conductivity. When the Li-ion concentration is increased, such as that in $Li_5La_3Nb_2O_{12}$ (33.34% Li(2) sites full) and $Li_7La_3Zr_2O_{12}$ (90% Li(2) sites full), the Li-ions on Li(1) sites remain stable but that on Li(2) sites are able to migrate from one site to the other. This migration of Li-ions between Li(2)-Li(2) sites passing their common tetrahedral Li(1) sites to give $Li_7La_3Zr_2O_{12}$ a very high Li-ion conductivity. The higher occupancy of Li(2) sites, > 90% Li(2) sites full for LLZO, although helpful in promoting more Li-ion transport, leaves insufficient vacancies for ion migration. Therefore, Xu *et al.* advise against further increasing Li concentration to higher than 7 in the garnet structure materials. Similar conclusion was also drawn experimentally by Li *et al.* using Ta-substituted LLZO.[12] The high Li-ion conductivity in $Li_{7-x}La_3Zr_{2-x}Ta_xO_{12}$ indicates that the appropriate Li-ion concentration in LLZO for Li-ion transport is in the range $6.4 \leq x \leq 6.6$. The best ratio of Li-ion occupancy to vacancy of the octahedral sites in LLZO appears to be around 3 : 1.

Further researches on the development of LLZO were focused on obtaining cubic phase and optimize its Li-ion conductivity by using different substitutions while controlling the Li concentration in the LLZO structure in between 6.2 and 7, **Table 1**. The substitutions are mainly carried out on Li-sites by using Al^{3+} and Ga^{3+} and on Zr-sites by using Ta^{5+} and Nb^{5+}, **Figure 2 (a)**. For the Al-substituted LLZO, the highest total conductivity is reported by Kumazaki *et al.* for 6.8×10^{-4} $S\cdot cm^{-1}$ at 25 °C.[13] Their ICP result shows that the sample contains 1.7 ^{wt}% Al and 0.1 ^{wt}% Si due to the contamination from used SiO_2 milling ball and Al_2O_3 crucible. Selected-area electron diffraction (SAED), electron energy-loss spectroscopy (EELS) were used to determine the presence of crystallites of $LiAl_5O_8$ and $LiAlSiO_4$ at the grain boundaries that facilitate the Li-ion transport across the grain boundaries and increase the total conductivity of the sample, **Figure 2(b)**.[13-14] Similar to Al-substitution, the substitution of Ga^{3+} also replace the Li-ions in LLZO. The highest reported total conductivity by using Ga-substitution is 1.84×10^{-3} $S\cdot cm^{-1}$ for $Li_{6.65}Ga_{0.15}La_3Zr_{1.9}Sc_{0.1}O_{12}$ at 27 °C.[15] Although the substitution of Ga^{3+} to Li-sites also obstructs the Li^+ percolation network, as that for Al-substitution, ^{71}Ga NMR shows that Ga^{3+} has preferential occupation of tetrahedral *24d* Li(1) sites over the distorted octahedral *96h* Li(2) sites, **Figure 2(c)**. Furthermore, theoretical calculations based on density functional theory and force-field-based molecular dynamic simulations suggest that the lower Ga^{3+}-Li^+ repulsion allows Li-ions more easily to diffuse within their immediate surroundings than that for Al^{3+}-Li^+.[16-17] Therefore, the higher population of local mobility Li^+ on *96h* Li(2) sites with lower Coulombic repulsion from Ga^{3+} promotes the long-range diffusion of Li^+ in LLZO, which leading to the higher ionic conductivity and lower activation energy of the Ga-substituted LLZO.[15, 18-19] Comparing to the substitution of Al^{3+} and Ga^{3+}, the substitution of Fe^{3+} to Li-sites is much less studied even though the reported total conductivity of $Li_{6.4}Fe_{0.2}La_3Zr_2O_{12}$ is as high as 1.82×10^{-3} $S\cdot cm^{-1}$.[20] Rettenwander *et al.* studied $Li_{6.4}Fe_{0.2}La_3Zr_2O_{12}$ by using ^{57}Fe Mössbauer spectra to show that about 96% of the total substituted iron occurs as Fe^{3+} and 4% as Fe^{2+}, **Figure 2(d)**.[21] Roughly two-thirds of the Fe^{3+} are assigned to the tetrahedral site *24d* Li(1) sites and roughly one-quarter to a highly distorted site *96h* Li(2) sites in the garnet structure, which is similar to that of Ga^{3+} with *24d* Li(1) sites preferential occupation to explain its high total conductivity.[21] However, the Fe^{3+} in LLZO can be reduced to Fe^{2+} when in contact with metallic Li, which make it no suitable for solid electrolyte application.[22]

The researches on Zr-site substitutions are majorly done by using Ta^{5+} and Nb^{5+} with concentrations between 0.2 and 0.75 ^{mol}%. The resulting total conductivities are usually higher than that for Al-substituted ones because Zr-substitutions do not obstruct the Li^+ diffusion path within LLZO structure. The highest conductive Ta-substituted LLZO was reported by Baek *et al*. at 2013 by using spark plasma sintering (i.e. hot-pressing) process to sinter $Li_{6.87}La_{2.97}Zr_{1.60}Ta_{0.56}O_{12-\delta}$.[23] The sample show a total conductivity as high as 1.35×10^{-3} S·cm^{-1} at 25 °C. Similar results also reported by He *et al.* on a hot-pressed $Li_{6.375}La_3Zr_{1.375}Nb_{0.625}O_{12}$ which has the highest total conductivity of Nb-substituted LLZO for 1.37×10^{-3} S·cm^{-1} at 25 °C.[24] Other than Ta^{5+} and Nb^{5+}, elements such as Te^{6+}, W^{6+}, Sb^{5+} and Mo^{6+} were also used for Zr-site substitution, **Table 1**. However, the actual valence of these substituted-elements in the LLZO structure were never identified, which means the site occupations are based on the design of starting reagents and the use of Al_2O_3 crucible could play a big role on the final measured total conductivities. Nevertheless, the Te-substituted LLZO, i.e. $Li_{6.5}La_3Zr_{1.75}Te_{0.25}O_{12}$,[25] was reported to have a very high total conductivity of 1.02×10^{-3} S·cm^{-1} at 30 °C and that for W-substituted LLZO, i.e. $Li_{6.4}La_3Zr_{1.7}W_{0.3}O_{12}$, was 9.11×10^{-4} S·cm^{-1} at RT.[26]

In summary, the understanding of crystal structure and Li-ion diffusion mechanism of LLZO allows elaborative design of the material to increase its Li-ion conductivity to higher than 1×10^{-3} S·cm^{-1} at RT by using Ta^{5+}, Nb^{5+}, Ga^{3+}, Fe^{3+} or Te^{6+} substitutions. It is suggested that the conductivity is affected far more by Li-ion concentration than by different dopant elements or lattice parameters for which the appropriate Li-ion concentration in LLZO should be in the range of $6.4 \leq x \leq 6.6$. Nevertheless, how a substitution affects the local environment for allowing easier Li-ion diffusion and higher chemical stability toward metallic Li should also be considered for a higher Li-ion conductive LLZO.

Table 1. List of total conductivity and used crucible for LLZO with different substitutions.

Compound	σ_{Li+} at RT (S cm^{-1})	Sintering crucible	Reference
$Li_7La_3Zr_2O_{12}$ (1000 °C/air, tetragonal phase)	σ_b=1.63x10^{-6}, σ_{gb}=5.59 x10^{-7}	Al_2O_3	5

$Li_7La_3Zr_2O_{12}$(1230 °C/air)	2.44 x10^{-4}	Al_2O_3	3
Al-doped $Li_7La_3Zr_2O_{12}$(1200 °C/air, citric acid pyrolysis, additional 1.2 ^{wt}% Al)	2.0 x10^{-4}	Al_2O_3	27
$Li_7La_3Zr_2O_{12}$(1230 °C/air, 1.7wt% Al and 0.1wt% Si by ICP, $LiAl_5O_8$ and $LiAlSiO_4$ at GB)	6.8 x10^{-4}	Al_2O_3	14
Al-doped $Li_7La_3Zr_2O_{12}$(1230 °C/air, 1.7 ^{wt}% Al and 0.1 ^{wt}% Si by ICP; Li-Al-Si-O/$LiAlSiO_4$ at GB)	6.8 x10^{-4}	Al_2O_3	13
Al-doped $Li_7La_3Zr_2O_{12}$ (1000 °C/air, additional 1.25 ^{wt}% γ-Al_2O_3)	2.4 x10^{-4}	-	28
Al-doped $Li_7La_3Zr_2O_{12}$(1200 °C/air, sol-gel)	1.4 x10^{-4}	Al_2O_3	6
$Li_{6.24}Al_{0.24}La_3Zr_2O_{11.98}$(1000 °C/air, hot-pressing, Need Al>0.204 mole to stabilize cubic phase)	4.0 x10^{-4}	BN coated Al_2O_3	10
$Li_{6.4}Al_{0.2}La_3Zr_2O_{12}$(1200 °C/air)	3.41 x10^{-4}	Al_2O_3	29
$Li_{6.25}Al_{0.24}La_3Zr_2O_{12}$ (1200 °C/air, glycine-nitrate pyrolysis)	5.1 x10^{-4}	Al_2O_3	30
$Li_{6.15}Al_{0.2}La_3Zr_{1.75}Ta_{0.25}O_{12}$ (1050 °C, hot-pressing)	3.7 x10^{-4}	ZrO_2	31
$Li_{6.8}La_3Zr_{1.8}Ta_{0.2}O_{12}$ (1130 °C/air, additional 0.5 ^{at}% $NaHCO_3$ and α-Al_2O_3)	7.3 x10^{-4}	Al_2O_3	32
$Li_{6.75}La_3Zr_{1.75}Ta_{0.25}O_{12}$ (1050 °C, hot-pressing)	8.7 x10^{-4}	ZrO_2	31
$Li_{6.75}La_3Zr_{1.75}Ta_{0.25}O_{12}$ (1175 °C/air, additional 1 ^{wt}% Li_3PO_4)	7.2 x10^{-4}	-	33
$Li_{6.75}La_3Zr_{1.75}Ta_{0.25}O_{12}$ (1050 °C/air)	1.97 x10^{-4}	ZrO_2	34
$Li_{6.75}La_3Zr_{1.75}Ta_{0.25}O_{12}$ (1180 °C/air, citric acid pyrolysis)	5.2 x10^{-4}	Al_2O_3	35
$Li_{6.4}La_3Zr_{1.4}Ta_{0.3}Nb_{0.3}O_{12}$ (1150 °C/air)	6.06 x10^{-4}	Al_2O_3	36
$Li_{6.625}La_3Zr_{1.625}Ta_{0.375}O_{12}$ (1150 °C/air, additional ~ 1.8 ^{wt}% Al_2O_3)	4.09 x10^{-4}	Al_2O_3	37
$Li_{6.625}La_3Zr_{1.625}Ta_{0.375}O_{12}$ (1000 °C/air, additional 29 ^{mol}% Al)	5.2 x10^{-4}	Al free crucible	38
$Li_{6.6}La_3Zr_{1.6}Ta_{0.4}O_{12}$ (1150 °C/Ar, hot-pressing)	1.18 x10^{-3}	graphite	39
Ta-doped $Li_7La_3Zr_2O_{12}$ (1140 °C/air, additional 0.5 mole Ta per formula LLZO)	6.45 x10^{-4}	Pt	40
$Li_{6.5}La_3Zr_{1.5}Ta_{0.5}O_{12}$ (1100 °C/air, hot-pressing)	8.4 x10^{-4}	YSZ	41
$Li_{6.87}La_{2.97}Zr_{1.60}Ta_{0.56}O_{12-\delta}$ (1000 °C/Ar)	1.35x10^{-3}	graphite	23
$Li_{6.4}La_3Zr_{1.4}Ta_{0.6}O_{12}$ (1140 °C/air, 2.5 ^{wt}% Al by ICP)	1.0 x10^{-3}	Al_2O_3	12
$Li_{6.4}La_3Zr_{1.4}Ta_{0.6}O_{12}$ (1150 °C/air)	7.2 x10^{-4}	Al_2O_3	36
$Li_{6.4}La_3Zr_{1.4}Ta_{0.6}O_{12}$ (1250 °C/air)	6.4 x10^{-4}	MgO	42
$Li_{6.25}La_3Zr_{1.25}Ta_{0.75}O_{12}$ (1150 °C/air)	2.72 x10^{-4}	MgO	43
$Li_{6.75}La_3Zr_{1.75}Nb_{0.25}O_{12}$ (1200 °C/air)	8.0 x10^{-4}	-	44
$Li_{6.75}La_3Zr_{1.75}Nb_{0.25}O_{12}$ (1150 °C/air, sol-gel, 0.46 ^{wt}% Al_2O_3 by ICP)	5.69 x10^{-4}	Al_2O_3	45
$Li_{6.75}La_3Zr_{1.75}Nb_{0.25}O_{12}$ (1050 °C/air)	2.3 x10^{-4}	ZrO_2	34
$Li_{6.625}La3Zr_{1.625}Nb_{0.375}O_{12}$ (1150 °C/air, additional ~ 1.8 ^{wt}% Al_2O_3)	4.25 x10^{-4}	Al_2O_3	37
$Li_{6.5}La3Zr_{1.625}Nb_{0.5}O_{12}$ (1150 °C/air, additional ~ 1.8 ^{wt}% Al_2O_3)	4.5 x10^{-4}	Al_2O_3	37
$Li_{6.375}La_3Zr_{1.375}Nb_{0.625}O_{12}$ (1150 °C/Ar)	1.37 x10^{-3}	graphite	24
$Li_{6.25}La_3Zr_{1.25}Nb_{0.75}O_{12}$ (1150 °C/air)	2.03 x10^{-4}	MgO	43

$Li_{6.55}Ga_{0.15}La_3Zr_2O_{12}$ (1085 °C/dry O_2, citric acid pyrolysis)	1.3×10^{-3}	Al_2O_3	18
$Li_{6.65}Ga_{0.15}La_3Zr_{1.9}Sc_{0.1}O_{12}$ (1200 °C/dry O_2, citric acid pyrolysis)	1.8×10^{-3}	Al_2O_3	15
$Li_{6.15}Ga_{0.2}La_3Zr_{1.75}Ta_{0.25}O_{12}$ (1050 °C, hot-pressing)	4.1×10^{-4}	ZrO_2	31
$Li_{6.75}La_{2.8}Ga_{0.2}Zr_{1.75}Nb_{0.25}O_{12}$ (1050 °C/air)	2.28×10^{-4}	ZrO_2	34
$Li_{6.75}La_{2.8}Ga_{0.2}Zr_{1.75}Ta_{0.25}O_{12}$ (1000 °C/air)	1.64×10^{-4}	ZrO_2	34
$Li_{6.4}Ga_{0.2}La_3Zr_2O_{12}$ (1230 °C/air)	1.32×10^{-3}	Al_2O_3	17
$Li_{6.25}Ga_{0.25}La_3Zr_2O_{12}$ (1000 °C/air, hot-pressing)	3.5×10^{-4}	ZrO_2	46
$Li_{6.25}Ga_{0.25}La_3Zr_2O_{12}$ (1130 °C/N_2, flame spray pyrolysis)	1.3×10^{-3}	graphite	47
$Li_{6.25}Ga_{0.25}La_3Zr_2O_{12}$ (1100 °C/air)	1.46×10^{-3}	Al_2O_3	19
$Li_{6.2}Ga_{0.3}La_{2.95}Rb_{0.05}Zr_2O_{12}$ (1100 °C/air)	1.62×10^{-3}	Al_2O_3	48
$Li_{5.5}Ga_{0.5}La_3Zr_2O_{12}$ (1150 °C/air, first report on Li^+/H^+ exchange)	1.0×10^{-4}	ZrO_2	49
Ga doped- $Li_7La_3Zr_2O_{12}$ (1085 °C/air, co-precipitation, additional 1 mole Ga per formula of LLZO)	5.4×10^{-4}	Pt	50
$Li_{7.06}La_3Zr_{1.94}Y_{0.06}O_{12}$ (1200 °C/air)	8.1×10^{-4}	Al_2O_3	51
$Li_{7.06}La_3Zr_{1.94}Y_{0.06}O_{12}$ (1100 °C/air, tetragonal phase)	1.0×10^{-6}	Al_2O_3	52
$Li_{6.65}La_{2.75}Ba_{0.25}Zr_{1.4}Ta_{0.5}Nb_{0.1}O_{12}$ (1150 °C/air)	5.27×10^{-4}	Al_2O_3	36
$Li_{6.5}La_{2.9}Ba_{0.1}Zr_{1.4}Ta_{0.6}O_{12}$ (1150 °C/air)	8.34×10^{-4}	Pt–Au	53
$Li_{6.4}Fe_{0.2}La_3Zr_2O_{12}$ (1230 °C/air)	1.1×10^{-3}	-	22
$Li_{6.4}Fe_{0.2}La_3Zr_2O_{12}$ (1225 °C/air, sol-gel)	1.82×10^{-3}	Al_2O_3	20
$Li_{6.4}La_3Zr_{1.7}W_{0.3}O_{12}$ (1100 °C/air)	7.89×10^{-4}	Al_2O_3	54
$Li_{6.4}La_3Zr_{1.7}W_{0.3}O_{12}$ (1180 °C/air, additional 0.2 ^{wt}% SiO_2)	9.11×10^{-4}	ZrO_2	26
$Li_7La_{2.75}Ca_{0.25}Zr_{1.75}Ta_{0.25}O_{12}$ (1100 °C/Ar, hot-pressing, additional 1.5 ^{wt}% γ-Al_2O_3)	7.65×10^{-4}	graphite	55
$Li_{6.6}La_{2.6}Ce_{0.4}Zr_2O_{12}$ (1050 °C/Ar, hot-pressing)	1.44×10^{-5}	graphite	56
$Li_{7.2}La_3Zr_{1.8}Gd_{0.2}O_{12}$ (1220 °C/air)	2.3×10^{-4}	-	57
Ge-doped $Li_7La_3Zr_2O_{12}$ (1200 °C/air, additional 1 ^{wt}% GeO_2)	7.63×10^{-4}	-	58
$Li_{6.6}La_3Zr_{1.8}Mo_{0.2}O_{12}$ (1100 °C/air, citric acid pyrolysis)	5.09×10^{-4}	Al_2O_3	59
$Li_7La_2NdZr_2O_{12}$ (1200 °C/air, 45 ^{mol}% Al by ICP)	8.1×10^{-6}	Au coated Al_2O_3	60
$Li_{6.6}La_3Zr_{1.6}Sb_{0.4}O_{12}$ (1100 °C/air)	7.7×10^{-4}	Al_2O_3	61
Sr-doped $Li_7La_3Zr_2O_{12}$ (1200 °C/air, additional 1.7 ^{wt}% Sr)	5.0×10^{-4}	Al_2O_3	62
$Li_{6.5}La_3Zr_{1.75}Te_{0.25}O_{12}$ (1100 °C/air)	1.03×10^{-3}	Al_2O_3	25

2.2 LLZO Chemical Stability toward Metallic Li

LLZOs are generally regarded as stable solid electrolytes when in contact with metallic Li. From a theoretical investigation, Zhu *et al*. use density functional theory calculations to show that LLZO has a very low reduction potential of 0.05 V vs. Li/Li^+ and a very small decomposition reaction energy of only 0.021 eV/atom (49 kJ/mol of LLZO) at 0 V vs. Li/Li^+**, Figure 3(a)**.[63] However, they further stated that their study cannot conclude if LLZO can be reduced by metallic Li or not because the small values of energy and voltage are below the typical accuracy of DFT and the approximations of the scheme. Experimentally, it is found that the chemical stability of LLZO toward metallic Li is affected by its substitution elements. Nemori *et al*. observed that the interfaces between Nb-substituted LLZOs, i.e. $Li_{6.25}La_3Nb_{1.375}Sc_{0.625}O_{12}$ and $Li_{6.25}La_3Nb_{0.75}Zr_{1.25}O_{12}$, and Li metal were turned into black color after 60 days of in contact to each other while that for $Li_{6.25}La_3Ta_{1.375}Sc_{0.625}O_{12}$ and $Li_{6.25}La_3Ta_{0.75}Zr_{1.25}O_{12}$ were unchanged, **Figure 3(b)**.[43] The changing of the color for Nb-substituted LLZOs are attributed to the reduction of Nb^{5+} to lower valence states by metallic Li. Similar to Nb-substituted LLZOs, a black surface coloration at the interface between Fe-substituted LLZO and Li metal was also observed by Rettenwander *et al,* **Figure 3(c).**[22] Raman spectra and nanosecond laser-induced breakdown spectroscopy were further used to reveal the formation of a Li-deficient tetragonal LLZO interlayer at the interface between Fe-substituted LLZO and metallic Li due to the reduction of Fe^{3+} to Fe^{2+}.

Different from Nb- and Fe-substituted LLZO for which the reduced interfaces can propagate through the material due to the formation of mixed conductors, a cubic phase Al-substituted LLZO, $Li_{6.25}Al_{0.25}La_3Zr_2O_{12}$, was found that it can be reduced by metallic Li and is accompanied by the simultaneous implantation of Li-ions into its structure, **Figure 4(a)**.[64] The findings from aberration-corrected scanning transmission electron microscope show that the implantation of Li-ions into the cubic phase LLZO results in a tetragonal phase LLZO interphase that stabilizes at an extremely small thickness of around five unit LLZO cells. This interphase also effectively prevented further interfacial reactions for cubic phase LLZO. Further experiments were carried out by Zhu *et al*. using X-ray photoelectron spectroscopy and impedance spectroscopy for understanding the origins of electrochemical stability of

LLZO by systematically studying both surface chemistry and substitution-dependent LLZO/Li interfacial reactivity.[65] The XPS results show that Zr^{4+} at the surface in all Al-, Ta- and Nb-substituted LLZOs were able to be reduced by metallic Li with the extent of reduction increasing as Ta < Nb < Al and the formation of an "oxygen-deficient interphase" layer that protects LLZO from further reduction, **Figure 4(b)**. Nevertheless, the Nb-ions in Nb-substituted LLZO have a thermodynamic preference to segregate to the LLZO surface and an even stronger preference to the Li/LLZO interface, whereas Ta dopants are nearly isoenergetic in the bulk and at the interface. This preference for surface segregation destabilize the formation of the "oxygen-deficient interphase" and allows the reduction reaction to propagate into the bulk of Nb-substituted LLZO, as the reason for observing the black coloration interface by Nemori *et al*.

It can be concluded that the chemical stability of LLZO toward metallic Li is highly depending on the substitution-elements. It is more likely that substitution of transition metals into LLZO could led to chemical instability of LLZO toward metallic Li. Even though Nb-substituted LLZO was long believed to be stable toward metallic Li, detail experiments show that the Nb-substituted LLZO is not stable when metallic Li is applied to its surface while Al- and Ta-substituted LLZO remain stable with the contact of metallic Li.

3. Negative Electrode Developments

Li-ion conductive ceramics were once believed that they can suppress Li dendrite formation due to their intrinsic high toughness, especially the shear modulus of LLZO is as high as ~ 55 GPa and its Li-ion transfer number is ~1.[8, 66] With the replacement of graphite by Li metal, it is expected that CLBs potentially offer a 70% increase of volumetric energy density and 40% increase of gravimetric energy density of the battery.[1-2] However, abrupt drops of polarization voltages were reported from several groups when cycling Li/LLZO/Li symmetric cells by direct current polarizations.[35, 39, 45, 67-68] Later, directly observations of Li propagation through LLZO along the grain boundaries were confirmed by using different characterization techniques such as high-resolution transmission electron microscopy combine with electron energy loss spectroscopy and scanning electron microscopy, **Figure 5(a)**.[39, 69-70]

The formation of Li dendrite in LLZO is recognized as a result of inhomogeneous contact between LLZO and Li electrode rather than as a consequence of low relative density of the used solid electrolytes.[39, 71] When inhomogeneous contact is formed, the high "effective current density" at the point contacts could electrochemically deposit metallic Li at defects to open up the rigid LLZO and propagate through the sample as shown by Porz *et al*. in both polycrystalline and single crystal LLZOs, **Figure 5(b)**.[72] Research efforts are, therefore, focusing on reducing the inhomogeneous contacts, which usually accompany with high interface resistance, between LLZO and Li electrode by using (I) interlayer coatings or (II) diminishing surface impurities. It is worth to mention that the surfaces of LLZOs for the interlayer coating experiments always need to be freshly polished in either air or inert atmosphere before depositing the interlayer. The Li electrode is usually applied at a temperature higher than the Li melting point. On the other hand, the experiments using diminishing surface impurities for reducing interface resistance usually need to apply a stack pressure to the symmetric cells at a temperature right below Li melting point for some hours to ensure the contact between LLZO and Li electrode, **Table 2**.

The interlayer coating was first proposed by Tsai *et al*. who use a thin Au interlayer to improve the contact between LLZO and Li electrodes, **Figure 5(c)**.[39] Because the coating technologies, such as sputter, atomic layer deposition, and wet chemical coatings, can effectively cover the whole surface of LLZO, the working principle of using interlayer coating is to take the advantage from the applied material which is able to in situ forming alloy with metallic Li to cover the surface of LLZO homogeneously. The interface resistance between LLZO and Li electrode was dramatically reduced from ~1500 $\Omega\cdot\text{cm}^2$ to 64 $\Omega\cdot\text{cm}^2$ by the thin layer Au coating, which results in short-circuit-free cells when running a direct current density of 0.5 $\text{mA}\cdot\text{cm}^{-2}$ through the LLZO pellets. Since then, various materials, such as Al, Al_2O_3, ZnO, Mg, Si, Sn, $AgNO_3$ and graphite, have been applied as the interlayer coatings for reducing the interface resistance between LLZO and Li, **Table 2**. Among all, the using of Li-Al alloy was reported that it can effectively reduce the interface resistance to as low as $< 1\ \Omega\cdot\text{cm}^2$.[73]

Most of the publications that using interlayer coatings to reduce interface resistance often show the wettability of between LLZO and metallic Li is low without their coatings. However, the low wettability between LLZO and metallic Li was found due to the formation of Li_2CO_3 at the surface of LLZO from Li^+/proton exchange when the sample was exposed to ambient environment.[68, 71, 74] The formation of Li_2CO_3 also block the Li-ion diffusion paths to give high interface resistance since Li_2CO_3 is not a good Li-ion conductor. Nevertheless, the formation of Li_2CO_3 can be erased by fine polish or acid etching of the surface of LLZO or restore the Li-ions from Li_2CO_3 back to LLZO by heating the sample under an inert atmosphere at a temperature higher than 250 °C, **Figure 5 (d)**.[75-76] Sharafi *et al.* further show that LLZO and Li can wet each other very well to give an interface resistance as low as 2 $\Omega \cdot cm^2$ by fine polishing the surface of LLZO in Ar atmosphere which followed by a heat treatment of the LLZO at 500 °C in an inert atmosphere to remove Li_2CO_3, **Figure 5(e)**.[71] Nevertheless, a stack pressure of 350 kPa at 175 °C is needed to apply to their symmetric cell for 12 hours to ensure a good contact between LLZO and Li electrode. More recently, Zheng *et al*. reported that the removing of impurity on the surface of used metallic Li, such as Li_2O, is as important as that on the surface of LLZO.[77] By ensuring an impurity-free at the interface between LLZO and Li, Zheng *et al*. show that the interface resistance can be diminished to 6.95 $\Omega \cdot cm^2$ which allows a Li/LLZO/Li symmetric cell to cycle with a high current density of 13.3 $mA \cdot cm^2$ for ~100 seconds per cycle step, i.e. 0.4 mA h cm^{-2}, or 2.2 $mA \cdot cm^2$ for 24 minutes per cycle step, i.e. 0.88 mA h cm^{-2}, **Figure 6(a)**.

Table 2. List of interface modifications and symmetric cell test conditions for LLZOs.

Solid Electrolyte	Interface Treatment (Li)	Interface Resistance ($\Omega \cdot cm^{-2}$)	Operation conductions (I density; step time; test temp.)	Used Li thickness (μm)	Reference
$Li_{6.5}La_3Zr_{1.5}Ta_{0.5}O_{12}$ (2D)	fine polish and Au interlayer (175 °C)	< 10	1 $mA \cdot cm^{-2}$; 3 hour/step; 60 °C	14.32	78
$Li_{6.4}La_3Zr_{1.4}Ta_{0.6}O_{12}$ (2D)	Remove Li_2O on Li (300 °C)	6.95	2.2 $mA \cdot cm^{-2}$; 0.4 hour/step; RT	4.2	77
$Li_{6.6}La_3Zr_{1.6}Ta_{0.4}O_{12}$ (2D)	150k Pa pressure with 100 C pre-cycle (175 °C)	58	0.1 $mA \cdot cm^{-2}$; 4 hour/step; 25 °C	1.909	79
$Li_{5.9}Al_{0.2}La_3Zr_{1.75}W_{0.25}O_{12}$ (2D)	Graphite interlayer (210 °C)	25	0.3 $mA \cdot cm^{-2}$; 1 hour/step; RT	1.432	80
$Li_{6.55}La_3Zr_{1.55}Ta_{0.45}O_{12}$ (2D)	Heat treatment (175 °C)	25	0.3 $mA \cdot cm^{-2}$; 1 hour/step; 25 °C	1.432	81
$Li_{6.5}La_3Zr_{1.5}Ta_{0.5}O_{12}$ (2D)	Li_3PO_4 interlayer (200 °C)	7	0.5 $mA \cdot cm^{-2}$; 0.5 hour/step; 25 °C	1.193	82

$Li_{6.375}La_3Zr_{1.375}Nb_{0.625}O_{12}$ (2D)	Sn interlayer (184 °C)	46.6	0.5 mA·cm^{-2}; 0.5 hour/step; 25 °C	1.193	24
$Li_{6.5}La_3Zr_{1.5}Ta_{0.5}O_{12}$ (2D)	$AgNO_3$ interlayer (220 °C)	4.5	0.5 mA·cm^{-2}; 0.5 hour/step; 25 °C	1.193	83
$Li_{6.25}Al_{0.25}La_3Zr_2O_{12}$ (2D)	Fine polish (175 °C)	2	0.2 mA·cm^{-2}; 1 hour/step; RT	0.955	71
$Li_{6.4}La_3Zr_{1.4}Ta_{0.6}O_{12}$ (2D)	Silica interlayer (185 °C)	49	0.2 mA·cm^{-2}; 1 hour/step; 24 °C	0.955	84
$Li_{6.6}La_3Zr_{1.6}Ta_{0.4}O_{12}$ (2D)	Au interlayer (100 °C)	64	0.08 mA·cm^{-2}; 2 hour/step; 25 °C	0.764	39
$Li_{6.5}La_3Zr_{1.5}Ta_{0.5}O_{12}$ (2D)	Surface rughness (thermal eva. Li)	363	0.3 mA·cm^{-2}; 0.5 hour/step; 25 °C	0.716	85
$Li_{6.4}La_3Zr_{1.4}Ta_{0.6}O_{12}$ (2D)	BN nanosheets interlayer (260 °C)	9	0.3 mA·cm^{-2}; 0.5 hour/step; RT	0.716	86
$Li_{6.4}La_3Zr_{1.5}Ta_{0.6}O_{12}$ (2D)	flake-graphite coating layer (230 °C)	40	0.1 mA·cm^{-2}; 1 hour/step; ? °C	0.477	87
$Li_7La_{2.75}Ca_{0.25}Zr_{1.75}Nb_{0.25}O_{12}$ (2D)	Al_2O_3 interlayer (250 °C)	34	0.2 mA·cm^{-2}; 0.5 hour/step; 25 °C	0.477	88
$Li_{6.4}La_3Zr_{1.4}Ta_{0.6}O_{12}$ (2D)	Au interlayer (250 °C)	3	0.3 mA·cm^{-2}; 0.33 hour/step; 25 °C	0.477	42
$Li_{6.5}La_3Zr_{1.5}Ta_{0.5}O_{12}$ (2D)	Al_4Li_9 alloy (250 °C)	< 1	0.2 mA·cm^{-2}; 0.17 hour/step; 25 °C	0.162	73
$Li_7La_{2.75}Ca_{0.25}Zr_{1.75}Nb_{0.25}O_{12}$ (2D)	Si interlayer (200 °C)	127	0.2 mA·cm^{-2}; 0.17 hour/step; RT	0.162	89
$Li_7La_{2.75}Ca_{0.25}Zr_{1.75}Nb_{0.25}O_{12}$ (2D)	Sn-Li alloy (250 °C)	7	0.05 mA·cm^{-2}; 0.5 hour/step; ? °C	0.119	90
$Li_7La_{2.75}Ca_{0.25}Zr_{1.75}Nb_{0.25}O_{12}$ (3D)	ZnO interlayer (300 °C)	20	0.1 mA·cm^{-2}; 0.17 hour/step; ? °C	0.081	91
$Li_{6.5}La_{2.9}Ba_{0.1}Zr_{1.4}Ta_{0.6}O_{12}$ (2D)	ZnO interlayer (250 °C)	10	0.1 mA·cm^{-2}; 0.17 hour/step; 25 °C	0.081	92
$Li_7La_{2.75}Ca_{0.25}Zr_{1.75}Nb_{0.25}O_{12}$ (2D)	Al interlayer (200 °C)	75	0.2 mA·cm^{-2}; 0.08 hour/step; 60 °C	0.08	93
$Li_7La_{2.75}Ca_{0.25}Zr_{1.75}Nb_{0.25}O_{12}$ (2D)	Mg interlayer (300 °C)	70	0.1 mA·cm^{-2}; 0.08 hour/step; 25 °C	0.04	94
$Li_7La_{2.75}Ca_{0.25}Zr_{1.75}Nb_{0.25}O_{12}$ (2D)	Ge interlayer (200 °C)	115	0.05 mA·cm^{-2}; 0.08 hour/step; RT	0.02	95
$Li_7La_{2.75}Ca_{0.25}Zr_{1.75}Nb_{0.25}O_{12}$ (3D)	ZnO interlayer (250 °C)	-	0.5 mA·cm^{-2}; 2 hour/step; ? °C	4.773	96
$Li_7La_{2.75}Ca_{0.25}Zr_{1.75}Nb_{0.25}O_{12}$ (3D)	ZnO interlayer (250 °C)	90	0.5 mA·cm^{-2}; 1 hour/step; ? °C	2.389	97

While all the papers claim that their method could effectively suppress Li dendrite formation, the demonstrated cycle performance by using Li/LLZO/Li symmetric cells are only able to deliver capacities much lower than a practical one, i.e. the used Li thicknesses are much thinner than 14.3 μm or $\ll$ 3 mA h·cm^{-2} in energy density, unless the operational temperature was increased to 60 °C,[78] **table 2**. At here, it is important to notice that some reports of galvanostatic cycling of Li symmetric cells with high current densities and capacities are in fact the result of "soft shorts" (stable electronic connections between the Li electrodes) as suggested by Albertus *et al*.[1] The reliability of the reported results can be easily examined by using Ohm's law to calculate the cell resistance, which should not be lower than the resistance from the used solid electrolyte itself. Therefore, it can be expected that there are more mechanisms hindering the use of metallic Li as the negative electrode for CLB. By measuring pressure-dependent electrode kinetics, Krauskopf *et al*. show that the vacancy diffusion limitation in the Li metal restricts the rate capability of the Li electrode because of contact loss caused by vacancy accumulation and the resulting pore formation near the interface, **Figure 6(b, c)**.[98] They further concluded that the interface between LLZO and Li would only remain morphologically stable when an applied current density is lower than 100 $\mu A \cdot cm^{-2}$ from a theoretical calculation based on their experimental results. This low current density means a planar geometry Li electrode is not high enough for practical cell application. How to resolve the diffusion limitation, e.g. increase Li diffusion coefficient by dopants, would be the next challenge for the Li electrode development for CLB.

4. **Positive Electrode Developments**

The compatibilities between LLZO and different positive active electrode materials near LLZO sintering temperature, i.e. ~ 1000 °C, are serving as the key factors for CLB fabrications due to the necessary of high temperature sintering process to form low resistive ionic diffusion paths. Positive active electrode materials including $LiMn_2O_4$, $LiFePO_4$, $LiCoMnO_4$, $LiFe_{0.5}Mn_{1.5}O_4$, $LiNi_{0.5}Mn_{1.5}O_4$, $LiNi_{1/3}Co_{1/3}Mn_{1/3}O_2$ and $LiCoO_2$ (LCO) had been examined for their compatibilities with LLZO at elevated temperatures.[99-104] X-ray diffraction (XRD) results show that $LiMn_2O_4$, $LiFePO_4$, $LiCoMnO_4$, $LiFe_{0.5}Mn_{1.5}O_4$ and $LiNi_{0.5}Mn_{1.5}O_4$ reacted with LLZO at temperatures between 400 and 600 °C while $LiNi_{1/3}Co_{1/3}Mn_{1/3}O_2$ is stable up to 800 °C. First principle calculations suggest that the decomposition of the positive active electrode materials act as oxidizers for the decomposition of LLZO.[100] Therefore, the low reaction temperatures make these materials difficult to be used in the traditionally high temperature sintering process for CLB fabrication.

The experimental results for the compatibility between LLZO and LCO are rather diverse. A closer examination of the reported publications can found that amorphous Li-Co-O precursors, which deposited by technologies such as plused laser depositions, physical vapor depositions and sol-gel methods, has a much lower reaction temperature with LLZO, ~ 700 °C, than those for using crystalline LCO, ~1085 °C.[102-104] Kim *et al*. suggest that La_2CoO_4 is the reaction byproduct at the interface of their pulsed laser deposited (PLD) Li-Co-O and LLZO, **Figure 7(a)**.[103] It is worth to note that the Li-Co-O film was deposit directly on LLZO at 700 °C by PLD. Therefore, it is reasonable to deduce that the formation of Li_2CoO_4 is highly correlative to the vacuum environment because Co^{2+} is not a stable state for cobalt when it is in a high temperature and oxygen rich environment.

When crystalline LCO is considered, Wakasugi *et al*. reported that the XRD patterns and charge-discharge behavior of a LCO and $Li_{6.25}Al_{0.25}La_3Zr_2O_{12}$ mixture did not change after the heat treatment at 800 °C by using ethylene carbonate/ethyl methyl carbonate/$LiPF_6$ liquid electrolyte.[99] Nevertheless, a detail study by using TEM and SIMS show that Al^{3+} in Al-substituted LLZO has preference to diffuse into LCO when the LLZO/LCO mixture was calcined at 700 °C, **Figure 7(b)**.[102] The departure of Al^{3+} from Al-substituted LLZO surface transformed cubic phase LLZO into the tetragonal phase one, which leading to a high interfacial resistance due to the low ionic conductivity of tetragonal phase LLZO. On the other hand, Uhlenbruck *et al*. reported that a rapid reaction between $Li_{6.75}La_3Zr_{1.6}Ta_{0.4}O_{12}$ (LLZTaO) and crystalline LCO only takes place at a temperature of 1085 °C by using XRD and differential scanning calorimetry measurement.[104] Later, Tsai *et al*. confirmed LLZTaO and crystalline LCO are chemically stable to each other up to 1050 °C by using micro-Raman mapping of their sintered LCO/LLZTaO composite electrode, **Figure 7(c)**.[105] Although a reaction byproduct, $LaCoO_3$, was reported to give an extra Raman band at 691 cm^{-1} when crystalline LCO and $Li_{6.75}La_3Zr_{1.75}Ta_{0.25}O_{12}$ was heat up to 900 °C,[101] Tsai *et al*. further verified that the extra peak at 693 cm^{-1} is due to a small concentration of Co^{3+} diffused into LLZTaO to give a photoluminescence peak at 693 cm^{-1} by using Co-substituted LLZO.

To summarize the compatibility between LCO and LLZO, it is reasonable to give a conclusion that amorphous Li-Co-O has a higher Gibbs free energy than that for crystalline LCO, which makes amorphous Li-Co-O more reactive to LLZO than crystalline LCO at lower temperatures. When a mixture of crystalline

LCO and LLZO is examined, the elemental substitution to LLZO could affect its chemical stability to LCO, where Ta-substituted LLZO has better chemical stability than Al-substituted LLZO.

CLB fabrications can be classified into two different approaches when using garnet structured LLZO solid electrolyte. One of the class is using thin film technologies such as pulsed laser deposition,[106-107] sputter deposition[28] and sol-gel deposition[108-109] to deposit active electrode materials on dense LLZO pellets to form CLBs. The results demonstrate electrochemical reactions from the deposited LCO but the areal capacities were very low, due to their low loadings and utilizations of LCO from lacking of Li-ion diffusion paths. These results are good to demonstrate the possibility of using LLZO to fabricate functional CLB but not for the practical due to the use of very thick LLZO solid electrolytes that gives their energy densities too low to be used at anywhere, **Table 3**.

The other type of batteries can be classified as "bulk-type" CLBs due to the use of casting method for composite positive electrode (CPE) fabrication or high yield deposition methods that are potentially able to achieve high energy densities. The most common approach of CPE fabrication is consisted of crystalline LCO and Li_3BO_3 (LBO) or its derivatives. In these CPEs, LBO is serving as a sintering additive which melts at 700 °C to cement LCO and LLZO together and provides Li-ion transport pathways across grain boundaries due to its very low Li-ion conductivity, ~ $2x10^{-6}$ S cm^{-1}, at RT, **Figure 8(a)**.[102, 110-116] The low melting point of LBO at 700 °C could effectively avoid the formation of highly resistive interface from the reaction between LLZO and LCO during high temperature sintering of CLB. These batteries offer very stable electrochemical performance up to 100 cycles but usually less than 10 cycles were shown in the publications**, Figure 8(b)** and **Table 3**. Another approach for making CPE was proposed by Tsai *et al*. by using crystalline LCO and LLZTaO, instead of using more reactive Li-Co-O precursors or Al-substituted LLZO, because both materials are chemically stable up to 1050 °C and do not form highly resistive tetragonal phase LLZO at the interface.[105] Their micro-Raman, energy-dispersive X-ray spectroscpoy mapping and cyclic voltammetry scan of fabricated CLB show that the well sintered interfaces are free from detrimental secondary phases that allows the CLB to increase its specific areal capacity for 10 times higher than other reports at 1.63 mA h cm^{-2} (i.e.110 mA h g^{-1}) with a much higher charge/discharge current density of 50 μA cm^{-2}, **Figure 8(c)**. The CLB also able to discharge at very high current densities up to 500 μA cm^{-2} at 50 °C due to the minimized cell areal resistance. However, the fabricated cell show a fast capacity degradation due to its microstructure failure from LCO breathing during charge/discharge cycling.

The other approach for preparing bulk-type CLBs is using aerosol deposition.[53, 117] Kato *et al.* fabricated their bulk-type CLB by using aerosol deposition that contains $LiNi_{1/3}Co_{1/3}Mn_{1/3}O_2$ +Li-Al-Ti-P-O glass ceramic as CPE to deposit on a LLZO pellet, **Figure 8(d)**.[117] The cell was able to deliver a high specific areal capacity of 0.5 mA h cm^{-2} and a high operational current density of 50 μA cm^{-2} at 100 °C. The same technology was used by Inada *et al.* to deposit $TiNb_2O_7$ thin film on LLZO. However, only one charge/discharge cycle was shown with relatively low current density, 2 μA·cm^{-2}, at 60° C in the report.[53] It is worth to mention that aerosol deposition has a major advantage of no need of high temperature sintering process when CLB is fabricated, which avoids the interface reaction between the used active electrode material and solid electrolyte. Therefore, a low interface resistance of constructed CLB can be expected by using this technology.

It is important to notice that the CLBs with very low specific areal loadings, usually < 2 mg cm^{-2}, and very low operational current densities, < 10 μA cm^{-2}, are good to demonstrate the proof of concepts but not able to show their potential for practical use in the future, **Table 3**. For example, the CLBs using LCO, LLZO and LBO as CPE were usually made with active electrode material loadings ~ 1 mg·cm^{-2} and operational current densities ~ 5 μA·cm^{-2}, **Table 3**. When the specific areal loading is increased, the electrochemical performance of this type of CLB is dramatically reduced by the low ionic conductivity of LBO and high tortuosity of Li-ion diffusion paths within the CPE as shown by Liu *et al.*[116] Although an argument of increasing specific areal capacity could simply be a technological issue instead of a scientific one, some physical problems such as establish of effective ionic diffusion paths, lower tortuosity for ionic diffusion, and reduce of microstructure fracture due to breathing behavior of active electrode materials may not able to be observed and solved easily for the cases with low active material loadings. Therefore, a demonstration of good CLB should contain reasonable active material loading to show that the electrochemical performance of the fabricated CLB can utilize most of the active materials from the CPE instead of only the materials on the interface, especially if the CLB is aiming for becoming a high energy density cell in the further.

Table 3. List of composition of positive electrode for all-ceramic Li batteries and their test conductions.

Composition	Active material loading (mg·cm^{-2})	Operation temp. (°C)	Operation Current density (μA·cm^{-2})	Specific areal capacity (mA h·cm^{-2})	Specific capacity (mA h·g^{-1})	No. of Cycles	Reference
$LiCoO_2/Li_3BO_3$/LLZO (composite)	-	RT	1 μA·g^{-1}	-	78	1	111
$LiCoO_2/Li_3BO_3$ (composite)	-	50	C/5	-	67.2	10	102
$LiMn_2O_4$/LLZO-0.3B_2O_3 (composite)	-	25	5	-	102.6	20	113
$LiCoO_2$ (sol-gel)	-	-	2	0.015	-	3	109
$LiCoO_2$ (PLD film, Nb-modified interface)	0.12	RT	1-10	0.01	80	25	106
V_2O_5/carbon nanotubes (composite)	0.2	100	10	0.03	150	27	118
$LiCoO_2$ (PLD film)	0.203	25	3.5	0.035	129	100	107
$TiNb_2O_7$ (aerosol deposition)	0.4	60	2	0.068	170	1	53
$Cu_{0.1}V_2O_5$/carbon (composite)	0.68	50	10	0.063	93	20	119
$Li(Ni_{0.5}Co_{0.2}Mn_{0.3})_{O2}$/ $In_{2(1-x)}Sn_{2x}O_3/Li_3BO_3$ (composite)	~1	80	5	0.123	123.3	5	114
$LiCoO_2/Li_2CO_3$ /$Li_{2.3}C_{0.7}B_{0.3}O_3$ (composite)	1	100	5.75	0.106	106	40	110
		25	5.75	0.094	94	100	
TiS_2/carbon nanotubes (composite)	1	150	300-1000	0.2	~200	400	120
$LiCoO_2$ (sputter)	1.52	RT	1	-	-	20	28
$LiCoO_2/Li_3BO_3/In2_{(1-x)}Sn_{2x}O_3$ (composite)	1.9	RT	5	0.19	101.3	5	115
$LiCoO_2$ thin Film (LiPON electrolyte)	2.02	25	46.5	0.106	50.3	100	121
$LiCoO_2/Li_3BO_3$ (composite)	2.35	25	10	0.2	85	5	112
$LiCoO_2$ (infiltrated sol-gel)	2.9	80	6.4	0.051	17.5	10	108
$LiCoO_2/Li_3BO_3/In2_{(1-x)}Sn_{2x}O_3$ (composite)	2.96	RT	5	0.056	13.9	6	116
$LiNi_{1/3}Co_{1/3}Mn_{1/3}O_2$/Li-Al-Ti-P-O (aerosol deposition)	3.7	100	50	0.5	135	90	117
$LiCoO_2$/LLZO (composite)	12.6	50	50	1.6	117	100	105

5. Summary and Perspectives

The discovery of fast Li-ion conductive garnet structured LLZO has been attracting much attention in electrochemical society due to their perspective of fabricating all-ceramic Li battery that gives much higher safety and energy density than conventional Li-ion batteries. After more than a decade of researching on LLZO, the understanding of the material properties has dramatically increased. On the development of LLZO, the accumulated knowledge has led to the increase of Li-ion conductivity for LLZO up to 1.8×10^{-3} $S\cdot cm^{-1}$ by substituting Fe or co-substituting Sc and Ga into LLZO. When using metallic Li as the negative electrode for CLB, detail researches found that the stability of LLZO toward metallic Li depends on the substituting elements, for which Ta shows the highest stability than Nb- and Al-substituted ones. Moreover, the high interface resistance between LLZO and Li electrode was found to be the consequence of impurity formations, such as Li_2CO_3, on the interface and inhomogeneous contact between LLZO and Li electrode. By carefully removing the impurities on the surface of LLZO and interlayer coatings, the interface resistance can be effectively reduced to a negligible number to relief the Li dendrite formation. Nevertheless, the Li dendrite problem is still lingered around when using metallic Li as the negative electrode. A depth investigation into the properties of metallic Li, such as atomic self-diffusion and mechanical properties, would be necessary for further solving the Li dendrite problem, especially the working principle of CLB is relying only on the solid-state diffusion mechanism. Although many publications have proposed different approaches for the positive electrode development, the active material loading and performance are still far away from a real application. Problems, such as internal elemental diffusion and high interface resistance, from conventional high temperature sintering process is still not yet fully understood and need to be solved. On the full CLB level, many data are still needed so that CLB performance can be optimized. For example, the knowledge on how to maximize the active material loading to achieve highest energy density, how the Li-ion percolation paths affect CLB performance, how to optimize the microstructure of CLB to accommodate the volume change of active material during charge/discharge cycling and even finding a more suitable positive electrode material for CLB development are still need to be fulfilled.

Acknowledgement

This work is financially supported by the project of "US-German Cooperation on Energy Storage" under the funding programs of "CatSe- Interfaces and Interphases in Rechargeable Li Based Batteries: Cathode/Solid Electrolyte" (Project No.: 13XP00223A) and "LISI- Lithium Solid Electrolyte Interfaces" (Project No.: 03XP0224B) from the Bundesministerium für Bildung und Forschung (BMBF).

References

(1) Albertus, P.; Babinec, S.; Litzelman, S.; Newman, A. Status and challenges in enabling the lithium metal electrode for high-energy and low-cost rechargeable batteries. *Nature Energy* **2017,** *3* (1), 16-21, DOI: 10.1038/s41560-017-0047-2.
(2) Janek, J.; Zeier, W. G. A solid future for battery development. *Nature Energy* **2016,** *1* (9), DOI: 10.1038/nenergy.2016.141.
(3) Murugan, R.; Thangadurai, V.; Weppner, W. Fast lithium ion conduction in garnet-type Li(7)La(3)Zr(2)O(12). *Angew Chem Int Ed Engl* **2007,** *46* (41), 7778-81, DOI: 10.1002/anie.200701144.
(4) Awaka, J.; Takashima, A.; Kataoka, K.; Kijima, N.; Idemoto, Y.; Akimoto, J. Crystal Structure of Fast Lithium-ion-conducting Cubic Li7La3Zr2O12. *Chemistry Letters* **2011,** *40* (1), 60-62, DOI: 10.1246/cl.2011.60.
(5) Awaka, J.; Kijima, N.; Hayakawa, H.; Akimoto, J. Synthesis and structure analysis of tetragonal Li7La3Zr2O12 with the garnet-related type structure. *Journal of Solid State Chemistry* **2009,** *182* (8), 2046-2052, DOI: 10.1016/j.jssc.2009.05.020.
(6) Li, Y.; Han, J.-T.; Wang, C.-A.; Vogel, S. C.; Xie, H.; Xu, M.; Goodenough, J. B. Ionic distribution and conductivity in lithium garnet Li7La3Zr2O12. *Journal of Power Sources* **2012,** *209*, 278-281, DOI: 10.1016/j.jpowsour.2012.02.100.
(7) Geiger, C. A.; Alekseev, E.; Lazic, B.; Fisch, M.; Armbruster, T.; Langner, R.; Fechtelkord, M.; Kim, N.; Pettke, T.; Weppner, W. Crystal chemistry and stability of "Li7La3Zr2O12" garnet: a fast lithium-ion conductor. *Inorg Chem* **2011,** *50* (3), 1089-97, DOI: 10.1021/ic101914e.
(8) Buschmann, H.; Dolle, J.; Berendts, S.; Kuhn, A.; Bottke, P.; Wilkening, M.; Heitjans, P.; Senyshyn, A.; Ehrenberg, H.; Lotnyk, A.; Duppel, V.; Kienle, L.; Janek, J. Structure and dynamics of the fast lithium ion conductor "Li7La3Zr2O12". *Phys Chem Chem Phys* **2011,** *13* (43), 19378-92, DOI: 10.1039/c1cp22108f.
(9) Bernstein, N.; Johannes, M. D.; Hoang, K. Origin of the structural phase transition in Li7La3Zr2O12. *Phys Rev Lett* **2012,** *109* (20), 205702, DOI: 10.1103/PhysRevLett.109.205702.
(10) Rangasamy, E.; Wolfenstine, J.; Sakamoto, J. The role of Al and Li concentration on the formation of cubic garnet solid electrolyte of nominal composition Li7La3Zr2O12. *Solid State Ionics* **2012,** *206*, 28-32, DOI: 10.1016/j.ssi.2011.10.022.

(11) Xu, M.; Park, M. S.; Lee, J. M.; Kim, T. Y.; Park, Y. S.; Ma, E. Mechanisms of Li+transport in garnet-type cubic Li3+xLa3M2O12(M= Te, Nb, Zr). *Physical Review B* **2012,** *85* (5), DOI: 10.1103/PhysRevB.85.052301.
(12) Li, Y.; Han, J.-T.; Wang, C.-A.; Xie, H.; Goodenough, J. B. Optimizing Li+ conductivity in a garnet framework. *Journal of Materials Chemistry* **2012,** *22* (30), DOI: 10.1039/c2jm31413d.
(13) Kumazaki, S.; Iriyama, Y.; Kim, K.-H.; Murugan, R.; Tanabe, K.; Yamamoto, K.; Hirayama, T.; Ogumi, Z. High lithium ion conductive Li7La3Zr2O12 by inclusion of both Al and Si. *Electrochemistry Communications* **2011,** *13* (5), 509-512, DOI: 10.1016/j.elecom.2011.02.035.
(14) Kim, K. H.; Hirayama, T.; Fisher, C. A. J.; Yamamoto, K.; Sato, T.; Tanabe, K.; Kumazaki, S.; Iriyama, Y.; Ogumi, Z. Characterization of grain-boundary phases in Li7La3Zr2O12 solid electrolytes. *Materials Characterization* **2014,** *91*, 101-106, DOI: 10.1016/j.matchar.2014.01.031.
(15) Buannic, L.; Orayech, B.; López Del Amo, J.-M.; Carrasco, J.; Katcho, N. A.; Aguesse, F.; Manalastas, W.; Zhang, W.; Kilner, J.; Llordés, A. Dual Substitution Strategy to Enhance Li+ Ionic Conductivity in Li7La3Zr2O12 Solid Electrolyte. *Chemistry of Materials* **2017,** *29* (4), 1769-1778, DOI: 10.1021/acs.chemmater.6b05369.
(16) Garcia Daza, F. A.; Bonilla, M. R.; Llordes, A.; Carrasco, J.; Akhmatskaya, E. Atomistic Insight into Ion Transport and Conductivity in Ga/Al-Substituted Li7La3Zr2O12 Solid Electrolytes. *ACS Appl Mater Interfaces* **2019,** *11* (1), 753-765, DOI: 10.1021/acsami.8b17217.
(17) Rettenwander, D.; Redhammer, G.; Preishuber-Pflugl, F.; Cheng, L.; Miara, L.; Wagner, R.; Welzl, A.; Suard, E.; Doeff, M. M.; Wilkening, M.; Fleig, J.; Amthauer, G. Structural and Electrochemical Consequences of Al and Ga Cosubstitution in Li7La3Zr2O12 Solid Electrolytes. *Chem Mater* **2016,** *28* (7), 2384-2392, DOI: 10.1021/acs.chemmater.6b00579.
(18) Bernuy-Lopez, C.; Manalastas, W.; Lopez del Amo, J. M.; Aguadero, A.; Aguesse, F.; Kilner, J. A. Atmosphere Controlled Processing of Ga-Substituted Garnets for High Li-Ion Conductivity Ceramics. *Chemistry of Materials* **2014,** *26* (12), 3610-3617, DOI: 10.1021/cm5008069.
(19) Wu, J. F.; Chen, E. Y.; Yu, Y.; Liu, L.; Wu, Y.; Pang, W. K.; Peterson, V. K.; Guo, X. Gallium-Doped Li7La3Zr2O12 Garnet-Type Electrolytes with High Lithium-Ion Conductivity. *ACS Appl Mater Interfaces* **2017,** *9* (2), 1542-1552, DOI: 10.1021/acsami.6b13902.
(20) Paulus, A.; Kammler, S.; Heuer, S.; Paulus, M. C.; Jakes, P.; Granwehr, J.; Eichel, R.-A. Sol Gel vs Solid State Synthesis of the Fast Lithium-Ion Conducting Solid State Electrolyte Li7La3Zr2O12Substituted with Iron. *Journal of The Electrochemical Society* **2019,** *166* (3), A5403-A5409, DOI: 10.1149/2.0641903jes.
(21) Rettenwander, D.; Geiger, C. A.; Amthauer, G. Synthesis and crystal chemistry of the fast Li-ion conductor Li7La3Zr2O12 doped with Fe. *Inorg Chem* **2013,** *52* (14), 8005-9, DOI: 10.1021/ic400589u.
(22) Rettenwander, D.; Wagner, R.; Reyer, A.; Bonta, M.; Cheng, L.; Doeff, M. M.; Limbeck, A.; Wilkening, M.; Amthauer, G. Interface Instability of Fe-Stabilized Li7La3Zr2O12 versus Li Metal. *J Phys Chem C Nanomater Interfaces* **2018,** *122* (7), 3780-3785, DOI: 10.1021/acs.jpcc.7b12387.
(23) Baek, S.-W.; Lee, J.-M.; Kim, T. Y.; Song, M.-S.; Park, Y. Garnet related lithium ion conductor processed by spark plasma sintering for all solid state batteries. *Journal of Power Sources* **2014,** *249*, 197-206, DOI: 10.1016/j.jpowsour.2013.10.089.

(24) He, M.; Cui, Z.; Chen, C.; Li, Y.; Guo, X. Formation of self-limited, stable and conductive interfaces between garnet electrolytes and lithium anodes for reversible lithium cycling in solid-state batteries. *Journal of Materials Chemistry A* **2018,** *6* (24), 11463-11470, DOI: 10.1039/c8ta02276c.

(25) Deviannapoorani, C.; Dhivya, L.; Ramakumar, S.; Murugan, R. Lithium ion transport properties of high conductive tellurium substituted Li7La3Zr2O12 cubic lithium garnets. *Journal of Power Sources* **2013,** *240*, 18-25, DOI: 10.1016/j.jpowsour.2013.03.166.

(26) Luo, Y.; Li, X.; Chen, H.; Guo, L. Influence of sintering aid on the microstructure and conductivity of the garnet-type W-doped Li7La3Zr2O12 ceramic electrolyte. *Journal of Materials Science: Materials in Electronics* **2019,** *30* (18), 17195-17201, DOI: 10.1007/s10854-019-02067-5.

(27) Jin, Y.; McGinn, P. J. Al-doped Li7La3Zr2O12 synthesized by a polymerized complex method. *Journal of Power Sources* **2011,** *196* (20), 8683-8687, DOI: 10.1016/j.jpowsour.2011.05.065.

(28) Kotobuki, M.; Kanamura, K.; Sato, Y.; Yoshida, T. Fabrication of all-solid-state lithium battery with lithium metal anode using Al2O3-added Li7La3Zr2O12 solid electrolyte. *Journal of Power Sources* **2011,** *196* (18), 7750-7754, DOI: 10.1016/j.jpowsour.2011.04.047.

(29) Tsai, C.-L.; Dashjav, E.; Hammer, E.-M.; Finsterbusch, M.; Tietz, F.; Uhlenbruck, S.; Buchkremer, H. P. High conductivity of mixed phase Al-substituted Li7La3Zr2O12. *Journal of Electroceramics* **2015,** *35* (1-4), 25-32, DOI: 10.1007/s10832-015-9988-7.

(30) Dhivya, L.; Karthik, K.; Ramakumar, S.; Murugan, R. Facile synthesis of high lithium ion conductive cubic phase lithium garnets for electrochemical energy storage devices. *RSC Advances* **2015,** *5* (116), 96042-96051, DOI: 10.1039/c5ra18543b.

(31) Allen, J. L.; Wolfenstine, J.; Rangasamy, E.; Sakamoto, J. Effect of substitution (Ta, Al, Ga) on the conductivity of Li7La3Zr2O12. *Journal of Power Sources* **2012,** *206*, 315-319, DOI: 10.1016/j.jpowsour.2012.01.131.

(32) Wang, Y.; Lai, W. High Ionic Conductivity Lithium Garnet Oxides of Li7−xLa3Zr2−xTaxO12 Compositions. *Electrochemical and Solid-State Letters* **2012,** *15* (5), DOI: 10.1149/2.024205esl.

(33) Cao, Y.; Li, Y.-Q.; Guo, X.-X. Densification and lithium ion conductivity of garnet-type Li7−xLa3Zr2−xTaxO12(x= 0.25) solid electrolytes. *Chinese Physics B* **2013,** *22* (7), DOI: 10.1088/1674-1056/22/7/078201.

(34) Gu, W.; Ezbiri, M.; Prasada Rao, R.; Avdeev, M.; Adams, S. Effects of penta- and trivalent dopants on structure and conductivity of Li7La3Zr2O12. *Solid State Ionics* **2015,** *274*, 100-105, DOI: 10.1016/j.ssi.2015.03.019.

(35) Ishiguro, K.; Nemori, H.; Sunahiro, S.; Nakata, Y.; Sudo, R.; Matsui, M.; Takeda, Y.; Yamamoto, O.; Imanishi, N. Ta-Doped Li7La3Zr2O12for Water-Stable Lithium Electrode of Lithium-Air Batteries. *Journal of The Electrochemical Society* **2014,** *161* (5), A668-A674, DOI: 10.1149/2.013405jes.

(36) Tong, X.; Thangadurai, V.; Wachsman, E. D. Highly conductive Li garnets by a multielement doping strategy. *Inorg Chem* **2015,** *54* (7), 3600-7, DOI: 10.1021/acs.inorgchem.5b00184.

(37) Huang, M.; Shoji, M.; Shen, Y.; Nan, C.-W.; Munakata, H.; Kanamura, K. Preparation and electrochemical properties of Zr-site substituted Li7La3(Zr2−xMx)O12 (M = Ta, Nb) solid electrolytes. *Journal of Power Sources* **2014,** *261*, 206-211, DOI: 10.1016/j.jpowsour.2014.03.070.

(38) Buschmann, H.; Berendts, S.; Mogwitz, B.; Janek, J. Lithium metal electrode kinetics and ionic conductivity of the solid lithium ion conductors “Li7La3Zr2O12” and Li7−xLa3Zr2−xTaxO12 with garnet-type structure. *Journal of Power Sources* **2012,** *206*, 236-244, DOI: 10.1016/j.jpowsour.2012.01.094.
(39) Tsai, C. L.; Roddatis, V.; Chandran, C. V.; Ma, Q.; Uhlenbruck, S.; Bram, M.; Heitjans, P.; Guillon, O. Li7La3Zr2O12 Interface Modification for Li Dendrite Prevention. *ACS Appl Mater Interfaces* **2016,** *8* (16), 10617-26, DOI: 10.1021/acsami.6b00831.
(40) Xia, W.; Xu, B.; Duan, H.; Tang, X.; Guo, Y.; Kang, H.; Li, H.; Liu, H. Reaction mechanisms of lithium garnet pellets in ambient air: The effect of humidity and CO2. *Journal of the American Ceramic Society* **2017,** *100* (7), 2832-2839, DOI: 10.1111/jace.14865.
(41) Naoki HAMAO; Kunimitsu KATAOKA; KIJIMA, N.; AKIMOTO, J. Synthesis, crystal structure and conductive properties of garnet-type lithium ion conductor Al-free Li7−xLa3Zr2−xTaxO12 (0 ≤ x ≤ 0.6). *Journal of the Ceramic Society of Japan* **2016,** *124* (6), P6-1-P6-3, DOI: 10.2109/jcersj2.124.P6-1.
(42) Huang, X.; Lu, Y.; Guo, H.; Song, Z.; Xiu, T.; Badding, M. E.; Wen, Z. None-Mother-Powder Method to Prepare Dense Li-Garnet Solid Electrolytes with High Critical Current Density. *ACS Applied Energy Materials* **2018,** *1*, 5355-5365, DOI: 10.1021/acsaem.8b00976.
(43) Nemori, H.; Matsuda, Y.; Mitsuoka, S.; Matsui, M.; Yamamoto, O.; Takeda, Y.; Imanishi, N. Stability of garnet-type solid electrolyte LixLa3A2-yByO12 (A=Nb or Ta, B=Sc or Zr). *Solid State Ionics* **2015,** *282*, 7-12, DOI: 10.1016/j.ssi.2015.09.015.
(44) Ohta, S.; Kobayashi, T.; Asaoka, T. High lithium ionic conductivity in the garnet-type oxide Li7−X La3(Zr2−X, NbX)O12 (X=0–2). *Journal of Power Sources* **2011,** *196* (6), 3342-3345, DOI: 10.1016/j.jpowsour.2010.11.089.
(45) Ishiguro, K.; Nakata, Y.; Matsui, M.; Uechi, I.; Takeda, Y.; Yamamoto, O.; Imanishi, N. Stability of Nb-Doped Cubic Li7La3Zr2O12with Lithium Metal. *Journal of The Electrochemical Society* **2013,** *160* (10), A1690-A1693, DOI: 10.1149/2.036310jes.
(46) Wolfenstine, J.; Ratchford, J.; Rangasamy, E.; Sakamoto, J.; Allen, J. L. Synthesis and high Li-ion conductivity of Ga-stabilized cubic Li7La3Zr2O12. *Materials Chemistry and Physics* **2012,** *134* (2-3), 571-575, DOI: 10.1016/j.matchemphys.2012.03.054.
(47) Yi, E.; Wang, W.; Kieffer, J.; Laine, R. M. Key parameters governing the densification of cubic-Li7La3Zr2O12 Li+ conductors. *Journal of Power Sources* **2017,** *352*, 156-164, DOI: 10.1016/j.jpowsour.2017.03.126.
(48) Wu, J. F.; Pang, W. K.; Peterson, V. K.; Wei, L.; Guo, X. Garnet-Type Fast Li-Ion Conductors with High Ionic Conductivities for All-Solid-State Batteries. *ACS Appl Mater Interfaces* **2017,** *9* (14), 12461-12468, DOI: 10.1021/acsami.7b00614.
(49) Howard, M. A.; Clemens, O.; Kendrick, E.; Knight, K. S.; Apperley, D. C.; Anderson, P. A.; Slater, P. R. Effect of Ga incorporation on the structure and Li ion conductivity of La3Zr2Li7O12. *Dalton Trans* **2012,** *41* (39), 12048-53, DOI: 10.1039/c2dt31318a.
(50) El Shinawi, H.; Janek, J. Stabilization of cubic lithium-stuffed garnets of the type “Li7La3Zr2O12” by addition of gallium. *Journal of Power Sources* **2013,** *225*, 13-19, DOI: 10.1016/j.jpowsour.2012.09.111.
(51) Murugan, R.; Ramakumar, S.; Janani, N. High conductive yttrium doped Li7La3Zr2O12 cubic lithium garnet. *Electrochemistry Communications* **2011,** *13* (12), 1373-1375, DOI: 10.1016/j.elecom.2011.08.014.

(52) Hitz, G. T.; Wachsman, E. D.; Thangadurai, V. Highly Li-Stuffed Garnet-Type Li7+xLa3Zr2-xYxO12. *Journal of The Electrochemical Society* **2013,** *160* (8), A1248-A1255, DOI: 10.1149/2.088308jes.
(53) Inada, R.; Yasuda, S.; Tojo, M.; Tsuritani, K.; Tojo, T.; Sakurai, Y. Development of Lithium-Stuffed Garnet-Type Oxide Solid Electrolytes with High Ionic Conductivity for Application to All-Solid-State Batteries. *Frontiers in Energy Research* **2016,** *4*, DOI: 10.3389/fenrg.2016.00028.
(54) Dhivya, L.; Janani, N.; Palanivel, B.; Murugan, R. Li+ transport properties of W substituted Li7La3Zr2O12 cubic lithium garnets. *AIP Advances* **2013,** *3* (8), DOI: 10.1063/1.4818971.
(55) Zhang, Y.; Hu, D.; Deng, J.; Chen, F.; Shen, Q.; Li, A.; Zhang, L.; Dong, S. Li+ transport channel size governing Li+ migration in garnet-based all-solid-state lithium batteries. *Journal of Alloys and Compounds* **2018,** *767*, 899-904, DOI: 10.1016/j.jallcom.2018.07.174.
(56) Rangasamy, E.; Wolfenstine, J.; Allen, J.; Sakamoto, J. The effect of 24c-site (A) cation substitution on the tetragonal–cubic phase transition in Li7−xLa3−xAxZr2O12 garnet-based ceramic electrolyte. *Journal of Power Sources* **2013,** *230*, 261-266, DOI: 10.1016/j.jpowsour.2012.12.076.
(57) Song, S.; Chen, B.; Ruan, Y.; Sun, J.; Yu, L.; Wang, Y.; Thokchom, J. Gd-doped Li7La3Zr2O12 garnet-type solid electrolytes for all-solid-state Li-Ion batteries. *Electrochimica Acta* **2018,** *270*, 501-508, DOI: 10.1016/j.electacta.2018.03.101.
(58) Huang, M.; Dumon, A.; Nan, C.-W. Effect of Si, In and Ge doping on high ionic conductivity of Li7La3Zr2O12. *Electrochemistry Communications* **2012,** *21*, 62-64, DOI: 10.1016/j.elecom.2012.04.032.
(59) Liu, X.; Li, Y.; Yang, T.; Cao, Z.; He, W.; Gao, Y.; Liu, J.; Li, G.; Li, Z. High lithium ionic conductivity in the garnet-type oxide Li7−2xLa3Zr2−xMoxO12 (x=0-0.3) ceramics by sol-gel method. *Journal of the American Ceramic Society* **2017,** *100* (4), 1527-1533, DOI: 10.1111/jace.14736.
(60) Hanc, E.; Zając, W.; Molenda, J. Synthesis procedure and effect of Nd, Ca and Nb doping on structure and electrical conductivity of Li7La3Zr2O12 garnets. *Solid State Ionics* **2014,** *262*, 617-621, DOI: 10.1016/j.ssi.2013.11.033.
(61) Ramakumar, S.; Satyanarayana, L.; Manorama, S. V.; Murugan, R. Structure and Li+ dynamics of Sb-doped Li7La3Zr2O12 fast lithium ion conductors. *Phys Chem Chem Phys* **2013,** *15* (27), 11327-38, DOI: 10.1039/c3cp50991e.
(62) Dumon, A.; Huang, M.; Shen, Y.; Nan, C.-W. High Li ion conductivity in strontium doped Li7La3Zr2O12 garnet. *Solid State Ionics* **2013,** *243*, 36-41, DOI: 10.1016/j.ssi.2013.04.016.
(63) Zhu, Y.; He, X.; Mo, Y. Origin of Outstanding Stability in the Lithium Solid Electrolyte Materials: Insights from Thermodynamic Analyses Based on First-Principles Calculations. *ACS Appl Mater Interfaces* **2015,** *7* (42), 23685-93, DOI: 10.1021/acsami.5b07517.
(64) Ma, C.; Cheng, Y.; Yin, K.; Luo, J.; Sharafi, A.; Sakamoto, J.; Li, J.; More, K. L.; Dudney, N. J.; Chi, M. Interfacial Stability of Li Metal-Solid Electrolyte Elucidated via in Situ Electron Microscopy. *Nano Lett* **2016,** *16* (11), 7030-7036, DOI: 10.1021/acs.nanolett.6b03223.
(65) Zhu, Y.; Connell, J. G.; Tepavcevic, S.; Zapol, P.; Garcia-Mendez, R.; Taylor, N. J.; Sakamoto, J.; Ingram, B. J.; Curtiss, L. A.; Freeland, J. W.; Fong, D. D.; Markovic, N. M. Dopant-Dependent Stability of Garnet Solid Electrolyte Interfaces with Lithium Metal. *Advanced Energy Materials* **2019,** *9* (12), DOI: 10.1002/aenm.201803440.

(66) Ni, J. E.; Case, E. D.; Sakamoto, J. S.; Rangasamy, E.; Wolfenstine, J. B. Room temperature elastic moduli and Vickers hardness of hot-pressed LLZO cubic garnet. *Journal of Materials Science* **2012,** *47* (23), 7978-7985, DOI: 10.1007/s10853-012-6687-5.
(67) Sudo, R.; Nakata, Y.; Ishiguro, K.; Matsui, M.; Hirano, A.; Takeda, Y.; Yamamoto, O.; Imanishi, N. Interface behavior between garnet-type lithium-conducting solid electrolyte and lithium metal. *Solid State Ionics* **2014,** *262*, 151-154, DOI: 10.1016/j.ssi.2013.09.024.
(68) Cheng, L.; Crumlin, E. J.; Chen, W.; Qiao, R.; Hou, H.; Franz Lux, S.; Zorba, V.; Russo, R.; Kostecki, R.; Liu, Z.; Persson, K.; Yang, W.; Cabana, J.; Richardson, T.; Chen, G.; Doeff, M. The origin of high electrolyte-electrode interfacial resistances in lithium cells containing garnet type solid electrolytes. *Phys Chem Chem Phys* **2014,** *16* (34), 18294-300, DOI: 10.1039/c4cp02921f.
(69) Cheng, E. J.; Sharafi, A.; Sakamoto, J. Intergranular Li metal propagation through polycrystalline Li6.25Al0.25La3Zr2O12 ceramic electrolyte. *Electrochimica Acta* **2017,** *223*, 85-91, DOI: 10.1016/j.electacta.2016.12.018.
(70) Matsuki, Y.; Noi, K.; Deguchi, M.; Sakuda, A.; Hayashi, A.; Tatsumisago, M. Lithium Dissolution/Deposition Behavior of Al-Doped Li7La3Zr2O12 Ceramics with Different Grain Sizes. *Journal of The Electrochemical Society* **2019,** *166* (3), A5470-A5473, DOI: 10.1149/2.0661903jes.
(71) Sharafi, A.; Kazyak, E.; Davis, A. L.; Yu, S.; Thompson, T.; Siegel, D. J.; Dasgupta, N. P.; Sakamoto, J. Surface Chemistry Mechanism of Ultra-Low Interfacial Resistance in the Solid-State Electrolyte Li7La3Zr2O12. *Chemistry of Materials* **2017,** *29* (18), 7961-7968, DOI: 10.1021/acs.chemmater.7b03002.
(72) Porz, L.; Swamy, T.; Sheldon, B. W.; Rettenwander, D.; Frömling, T.; Thaman, H. L.; Berendts, S.; Uecker, R.; Carter, W. C.; Chiang, Y.-M. Mechanism of Lithium Metal Penetration through Inorganic Solid Electrolytes. *Advanced Energy Materials* **2017,** *7* (20), DOI: 10.1002/aenm.201701003.
(73) Lu, Y.; Huang, X.; Ruan, Y.; Wang, Q.; Kun, R.; Yang, J.; Wen, Z. An in situ element permeation constructed high endurance Li–LLZO interface at high current densities. *Journal of Materials Chemistry A* **2018,** *6* (39), 18853-18858, DOI: 10.1039/c8ta07241h.
(74) Sharafi, A.; Yu, S.; Naguib, M.; Lee, M.; Ma, C.; Meyer, H. M.; Nanda, J.; Chi, M.; Siegel, D. J.; Sakamoto, J. Impact of air exposure and surface chemistry on Li–Li7La3Zr2O12 interfacial resistance. *Journal of Materials Chemistry A* **2017,** *5* (26), 13475-13487, DOI: 10.1039/c7ta03162a.
(75) Cheng, L.; Liu, M.; Mehta, A.; Xin, H.; Lin, F.; Persson, K.; Chen, G.; Crumlin, E. J.; Doeff, M. Garnet Electrolyte Surface Degradation and Recovery. *ACS Applied Energy Materials* **2018,** *1* (12), 7244-7252, DOI: 10.1021/acsaem.8b01723.
(76) Motoyama, M.; Tanaka, Y.; Yamamoto, T.; Tsuchimine, N.; Kobayashi, S.; Iriyama, Y. The Active Interface of Ta-Doped Li7La3Zr2O12 for Li Plating/Stripping Revealed by Acid Aqueous Etching. *ACS Applied Energy Materials* **2019,** *2* (9), 6720-6731, DOI: 10.1021/acsaem.9b01193.
(77) Zheng, H.; Wu, S.; Tian, R.; Xu, Z.; Zhu, H.; Duan, H.; Liu, H. Intrinsic Lithiophilicity of Li–Garnet Electrolytes Enabling High-Rate Lithium Cycling. *Advanced Functional Materials* **2019**, DOI: 10.1002/adfm.201906189.
(78) Taylor, N. J.; Stangeland-Molo, S.; Haslam, C. G.; Sharafi, A.; Thompson, T.; Wang, M.; Garcia-Mendez, R.; Sakamoto, J. Demonstration of high current densities and extended cycling

in the garnet Li7La3Zr2O12 solid electrolyte. *Journal of Power Sources* **2018,** *396*, 314-318, DOI: 10.1016/j.jpowsour.2018.06.055.
(79) Yonemoto, F.; Nishimura, A.; Motoyama, M.; Tsuchimine, N.; Kobayashi, S.; Iriyama, Y. Temperature effects on cycling stability of Li plating/stripping on Ta-doped Li7La3Zr2O12. *Journal of Power Sources* **2017,** *343*, 207-215, DOI: 10.1016/j.jpowsour.2017.01.009.
(80) Shao, Y.; Wang, H.; Gong, Z.; Wang, D.; Zheng, B.; Zhu, J.; Lu, Y.; Hu, Y.-S.; Guo, X.; Li, H.; Huang, X.; Yang, Y.; Nan, C.-W.; Chen, L. Drawing a Soft Interface: An Effective Interfacial Modification Strategy for Garnet-Type Solid-State Li Batteries. *ACS Energy Letters* **2018,** *3* (6), 1212-1218, DOI: 10.1021/acsenergylett.8b00453.
(81) Inada, R.; Yasuda, S.; Hosokawa, H.; Saito, M.; Tojo, T.; Sakurai, Y. Formation and Stability of Interface between Garnet-Type Ta-doped Li7La3Zr2O12 Solid Electrolyte and Lithium Metal Electrode. *Batteries* **2018,** *4* (2), DOI: 10.3390/batteries4020026.
(82) Ruan, Y.; Lu, Y.; Huang, X.; Su, J.; Sun, C.; Jin, J.; Wen, Z. Acid induced conversion towards a robust and lithiophilic interface for Li–Li7La3Zr2O12 solid-state batteries. *Journal of Materials Chemistry A* **2019,** *7* (24), 14565-14574, DOI: 10.1039/c9ta01911a.
(83) Cai, M.; Lu, Y.; Su, J.; Ruan, Y.; Chen, C.; Chowdari, B. V. R.; Wen, Z. In Situ Lithiophilic Layer from H(+)/Li(+) Exchange on Garnet Surface for the Stable Lithium-Solid Electrolyte Interface. *ACS Appl Mater Interfaces* **2019,** *11* (38), 35030-35038, DOI: 10.1021/acsami.9b13190.
(84) Liu, K.; Li, Y.; Zhang, R.; Wu, M.; Huang, B.; Zhao, T. Facile Surface Modification Method To Achieve an Ultralow Interfacial Resistance in Garnet-Based Li Metal Batteries. *ACS Applied Energy Materials* **2019,** *2* (9), 6332-6340, DOI: 10.1021/acsaem.9b00967.
(85) Basappa, R. H.; Ito, T.; Yamada, H. Contact between Garnet-Type Solid Electrolyte and Lithium Metal Anode: Influence on Charge Transfer Resistance and Short Circuit Prevention. *Journal of The Electrochemical Society* **2017,** *164* (4), A666-A671, DOI: 10.1149/2.0841704jes.
(86) Wen, J.; Huang, Y.; Duan, J.; Wu, Y.; Luo, W.; Zhou, L.; Hu, C.; Huang, L.; Zheng, X.; Yang, W.; Wen, Z.; Huang, Y. Highly Adhesive Li-BN Nanosheet Composite Anode with Excellent Interfacial Compatibility for Solid-State Li Metal Batteries. *ACS Nano* **2019,** *13* (12), 14549-14556, DOI: 10.1021/acsnano.9b08803.
(87) Sun, B.; Jin, Y.; Lang, J.; Liu, K.; Fang, M.; Wu, H. A painted layer for high-rate and high-capacity solid-state lithium-metal batteries. *Chem Commun (Camb)* **2019,** *55* (47), 6704-6707, DOI: 10.1039/c9cc02394a.
(88) Han, X.; Gong, Y.; Fu, K. K.; He, X.; Hitz, G. T.; Dai, J.; Pearse, A.; Liu, B.; Wang, H.; Rubloff, G.; Mo, Y.; Thangadurai, V.; Wachsman, E. D.; Hu, L. Negating interfacial impedance in garnet-based solid-state Li metal batteries. *Nat Mater* **2017,** *16* (5), 572-579, DOI: 10.1038/nmat4821.
(89) Luo, W.; Gong, Y.; Zhu, Y.; Fu, K. K.; Dai, J.; Lacey, S. D.; Wang, C.; Liu, B.; Han, X.; Mo, Y.; Wachsman, E. D.; Hu, L. Transition from Superlithiophobicity to Superlithiophilicity of Garnet Solid-State Electrolyte. *J Am Chem Soc* **2016,** *138* (37), 12258-62, DOI: 10.1021/jacs.6b06777.
(90) Wang, C.; Xie, H.; Zhang, L.; Gong, Y.; Pastel, G.; Dai, J.; Liu, B.; Wachsman, E. D.; Hu, L. Universal Soldering of Lithium and Sodium Alloys on Various Substrates for Batteries. *Advanced Energy Materials* **2018,** *8* (6), DOI: 10.1002/aenm.201701963.
(91) Wang, C.; Gong, Y.; Liu, B.; Fu, K.; Yao, Y.; Hitz, E.; Li, Y.; Dai, J.; Xu, S.; Luo, W.; Wachsman, E. D.; Hu, L. Conformal, Nanoscale ZnO Surface Modification of Garnet-Based

Solid-State Electrolyte for Lithium Metal Anodes. *Nano Lett* **2017,** *17* (1), 565-571, DOI: 10.1021/acs.nanolett.6b04695.

(92) Zhou, C.; Samson, A. J.; Hofstetter, K.; Thangadurai, V. A surfactant-assisted strategy to tailor Li-ion charge transfer interfacial resistance for scalable all-solid-state Li batteries. *Sustainable Energy & Fuels* **2018,** *2* (10), 2165-2170, DOI: 10.1039/c8se00234g.

(93) Fu, K. K.; Gong, Y.; Liu, B.; Zhu, Y.; Xu, S.; Yao, Y.; Luo, W.; Wang, C.; Lacey, S. D.; Dai, J.; Chen, Y.; Mo, Y.; Wachsman, E.; Hu, L. Toward garnet electrolyte–based Li metal batteries An ultrathin, highly effective, artificial solid-state electrolytemetallic Li interface. *SCIENCE ADVANCES* **2017,** *3*, e1601659.

(94) Fu, K. K.; Gong, Y.; Fu, Z.; Xie, H.; Yao, Y.; Liu, B.; Carter, M.; Wachsman, E.; Hu, L. Transient Behavior of the Metal Interface in Lithium Metal-Garnet Batteries. *Angew Chem Int Ed Engl* **2017,** *56* (47), 14942-14947, DOI: 10.1002/anie.201708637.

(95) Luo, W.; Gong, Y.; Zhu, Y.; Li, Y.; Yao, Y.; Zhang, Y.; Fu, K. K.; Pastel, G.; Lin, C. F.; Mo, Y.; Wachsman, E. D.; Hu, L. Reducing Interfacial Resistance between Garnet-Structured Solid-State Electrolyte and Li-Metal Anode by a Germanium Layer. *Adv Mater* **2017,** *29* (22), DOI: 10.1002/adma.201606042.

(96) Yang, C.; Zhang, L.; Liu, B.; Xu, S.; Hamann, T.; McOwen, D.; Dai, J.; Luo, W.; Gong, Y.; Wachsman, E. D.; Hu, L. Continuous plating/stripping behavior of solid-state lithium metal anode in a 3D ion-conductive framework. *Proc Natl Acad Sci U S A* **2018,** *115* (15), 3770-3775, DOI: 10.1073/pnas.1719758115.

(97) Liu, B.; Zhang, L.; Xu, S.; McOwen, D. W.; Gong, Y.; Yang, C.; Pastel, G. R.; Xie, H.; Fu, K.; Dai, J.; Chen, C.; Wachsman, E. D.; Hu, L. 3D lithium metal anodes hosted in asymmetric garnet frameworks toward high energy density batteries. *Energy Storage Materials* **2018,** *14*, 376-382, DOI: 10.1016/j.ensm.2018.04.015.

(98) Krauskopf, T.; Hartmann, H.; Zeier, W. G.; Janek, J. Toward a Fundamental Understanding of the Lithium Metal Anode in Solid-State Batteries-An Electrochemo-Mechanical Study on the Garnet-Type Solid Electrolyte Li6.25Al0.25La3Zr2O12. *ACS Appl Mater Interfaces* **2019,** *11* (15), 14463-14477, DOI: 10.1021/acsami.9b02537.

(99) Wakasugi, J.; Munakata, H.; Kanamura, K. Thermal Stability of Various Cathode Materials against Li_{6.25}Al_{0.25}La₃Zr₂O₁₂ Electrolyte. *Electrochemistry* **2017,** *85* (2), 77-81, DOI: 10.5796/electrochemistry.85.77.

(100) Miara, L.; Windmuller, A.; Tsai, C. L.; Richards, W. D.; Ma, Q.; Uhlenbruck, S.; Guillon, O.; Ceder, G. About the Compatibility between High Voltage Spinel Cathode Materials and Solid Oxide Electrolytes as a Function of Temperature. *ACS Appl Mater Interfaces* **2016,** *8* (40), 26842-26850, DOI: 10.1021/acsami.6b09059.

(101) Ren, Y.; Liu, T.; Shen, Y.; Lin, Y.; Nan, C.-W. Chemical compatibility between garnet-like solid state electrolyte Li6.75La3Zr1.75Ta0.25O12 and major commercial lithium battery cathode materials. *Journal of Materiomics* **2016,** *2* (3), 256-264, DOI: 10.1016/j.jmat.2016.04.003.

(102) Park, K.; Yu, B.-C.; Jung, J.-W.; Li, Y.; Zhou, W.; Gao, H.; Son, S.; Goodenough, J. B. Electrochemical Nature of the Cathode Interface for a Solid-State Lithium-Ion Battery: Interface between LiCoO2 and Garnet-Li7La3Zr2O12. *Chemistry of Materials* **2016,** *28* (21), 8051-8059, DOI: 10.1021/acs.chemmater.6b03870.

(103) Kim, K. H.; Iriyama, Y.; Yamamoto, K.; Kumazaki, S.; Asaka, T.; Tanabe, K.; Fisher, C. A. J.; Hirayama, T.; Murugan, R.; Ogumi, Z. Characterization of the interface between LiCoO2

and Li7La3Zr2O12 in an all-solid-state rechargeable lithium battery. *Journal of Power Sources* **2011,** *196* (2), 764-767, DOI: 10.1016/j.jpowsour.2010.07.073.

(104) Sven Uhlenbruck, J. D., Sandra Lobe, Christian Dellen, Chih-Long Tsai, Benjamin Gotzen, Doris Sebold, Martin Finsterbusch,Olivier Guillon. Cathode-electrolyte material interactions during manufacturing of inorganic solid-state lithium batteries. *J. Electroceram* **2017,** *38*, 197-206.

(105) Tsai, C.-L.; Ma, Q.; Dellen, C.; Lobe, S.; Vondahlen, F.; Windmüller, A.; Grüner, D.; Zheng, H.; Uhlenbruck, S.; Finsterbusch, M.; Tietz, F.; Fattakhova-Rohlfing, D.; Buchkremer, H. P.; Guillon, O. A garnet structure-based all-solid-state Li battery without interface modification: resolving incompatibility issues on positive electrodes. *Sustainable Energy & Fuels* **2019,** *3* (1), 280-291, DOI: 10.1039/c8se00436f.

(106) Kato, T.; Hamanaka, T.; Yamamoto, K.; Hirayama, T.; Sagane, F.; Motoyama, M.; Iriyama, Y. In-situ Li7La3Zr2O12/LiCoO2 interface modification for advanced all-solid-state battery. *Journal of Power Sources* **2014,** *260*, 292-298, DOI: 10.1016/j.jpowsour.2014.02.102.

(107) Ohta, S.; Kobayashi, T.; Seki, J.; Asaoka, T. Electrochemical performance of an all-solid-state lithium ion battery with garnet-type oxide electrolyte. *Journal of Power Sources* **2012,** *202*, 332-335, DOI: 10.1016/j.jpowsour.2011.10.064.

(108) Ren, Y.; Liu, T.; Shen, Y.; Lin, Y.; Nan, C.-W. Garnet-type oxide electrolyte with novel porous-dense bilayer configuration for rechargeable all-solid-state lithium batteries. *Ionics* **2017,** *23* (9), 2521-2527, DOI: 10.1007/s11581-017-2224-5.

(109) Masashi Kotobuki; Hirokazu Munakata; Yoshida, T. Compatibility of Li7La3Zr2O12 Solid Electrolyte to All-Solid-State Battery Using Li Metal Anode. *Journal of The Electrochemical Society* **2010,** *157* (10), A1076-A1079, DOI: 10.1149/1.3474232 兴.

(110) Han, F.; Yue, J.; Chen, C.; Zhao, N.; Fan, X.; Ma, Z.; Gao, T.; Wang, F.; Guo, X.; Wang, C. Interphase Engineering Enabled All-Ceramic Lithium Battery. *Joule* **2018,** *2* (3), 497-508, DOI: 10.1016/j.joule.2018.02.007.

(111) Ohta, S.; Seki, J.; Yagi, Y.; Kihira, Y.; Tani, T.; Asaoka, T. Co-sinterable lithium garnet-type oxide electrolyte with cathode for all-solid-state lithium ion battery. *Journal of Power Sources* **2014,** *265*, 40-44, DOI: 10.1016/j.jpowsour.2014.04.065.

(112) Ohta, S.; Komagata, S.; Seki, J.; Saeki, T.; Morishita, S.; Asaoka, T. All-solid-state lithium ion battery using garnet-type oxide and Li3BO3 solid electrolytes fabricated by screen-printing. *Journal of Power Sources* **2013,** *238*, 53-56, DOI: 10.1016/j.jpowsour.2013.02.073.

(113) Feng, L.; Li, L.; Zhang, Y.; Peng, H.; Zou, Y. Low temperature synthesis and ion conductivity of Li7La3Zr2O12 garnets for solid state Li ion batteries. *Solid State Ionics* **2017,** *310*, 129-133, DOI: 10.1016/j.ssi.2017.08.016.

(114) Liu, T.; Zhang, Y.; Zhang, X.; Wang, L.; Zhao, S.-X.; Lin, Y.-H.; Shen, Y.; Luo, J.; Li, L.; Nan, C.-W. Enhanced electrochemical performance of bulk type oxide ceramic lithium batteries enabled by interface modification. *Journal of Materials Chemistry A* **2018,** *6* (11), 4649-4657, DOI: 10.1039/c7ta06833f.

(115) Liu, T.; Zhang, Y.; Chen, R.; Zhao, S.-X.; Lin, Y.; Nan, C.-W.; Shen, Y. Non-successive degradation in bulk-type all-solid-state lithium battery with rigid interfacial contact. *Electrochemistry Communications* **2017,** *79*, 1-4, DOI: 10.1016/j.elecom.2017.03.016.

(116) Liu, T.; Ren, Y.; Shen, Y.; Zhao, S.-X.; Lin, Y.; Nan, C.-W. Achieving high capacity in bulk-type solid-state lithium ion battery based on Li 6.75 La 3 Zr 1.75 Ta 0.25 O 12 electrolyte: Interfacial resistance. *Journal of Power Sources* **2016,** *324*, 349-357, DOI: 10.1016/j.jpowsour.2016.05.111.

(117) Kato, T.; Iwasaki, S.; Ishii, Y.; Motoyama, M.; West, W. C.; Yamamoto, Y.; Iriyama, Y. Preparation of thick-film electrode-solid electrolyte composites on Li7La3Zr2O12 and their electrochemical properties. *Journal of Power Sources* **2016,** *303*, 65-72, DOI: 10.1016/j.jpowsour.2015.10.101.
(118) Liu, B.; Fu, K.; Gong, Y.; Yang, C.; Yao, Y.; Wang, Y.; Wang, C.; Kuang, Y.; Pastel, G.; Xie, H.; Wachsman, E. D.; Hu, L. Rapid Thermal Annealing of Cathode-Garnet Interface toward High-Temperature Solid State Batteries. *Nano Lett* **2017,** *17* (8), 4917-4923, DOI: 10.1021/acs.nanolett.7b01934.
(119) Jin, Y.; McGinn, P. J. Bulk solid state rechargeable lithium ion battery fabrication with Al-doped Li7La3Zr2O12 electrolyte and Cu0.1V2O5 cathode. *Electrochimica Acta* **2013,** *89*, 407-412, DOI: 10.1016/j.electacta.2012.11.059.
(120) Wang, C.; Zhang, L.; Xie, H.; Pastel, G.; Dai, J.; Gong, Y.; Liu, B.; Wachsman, E. D.; Hu, L. Mixed ionic-electronic conductor enabled effective cathode-electrolyte interface in all solid state batteries. *Nano Energy* **2018,** *50*, 393-400, DOI: 10.1016/j.nanoen.2018.05.062.
(121) Koo, M.; Park, K. I.; Lee, S. H.; Suh, M.; Jeon, D. Y.; Choi, J. W.; Kang, K.; Lee, K. J. Bendable inorganic thin-film battery for fully flexible electronic systems. *Nano Lett* **2012,** *12* (9), 4810-6, DOI: 10.1021/nl302254v.

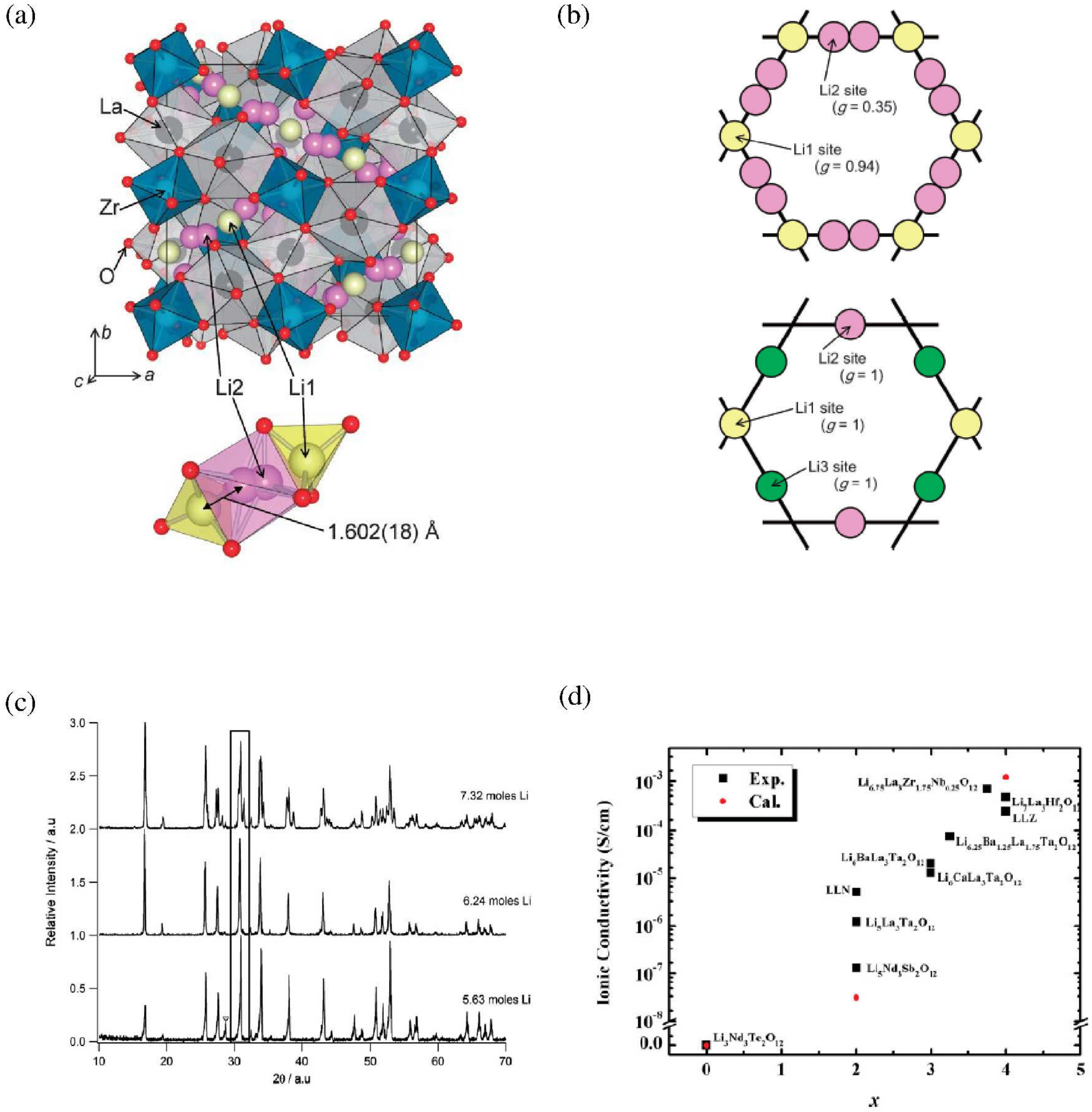

Figure 1. Development of LLZO based solid electrolyte. **(a)** Crystal structure of cubic $Li_7La_3Zr_2O_{12}$ (top) and coordination polyhedra around the Li(1) and Li(2) sites (bottom).[4] Reproduced with permission.[4] Copyright 2011, Elsevier. **(b)** The loop structures constructed by Li atomic arrangement in cubic (top) and tetragonal (bottom) $Li_7La_3Zr_2O_{12}$ with occupancy value g for each site in the parenthesis.[4] Reproduced with permission.[4] Copyright 2011, Elsevier. **(c)** A phase transition from cubic to tetragonal $Li_7La_3Zr_2O_{12}$ when Li increase from 6.24 mole to 7.32 mole.[10] Reproduced with permission.[10] Copyright 2012, Elsevier. **(d)** The effect of Li-ion concentration to bulk ionic conductivities in various garnet-type $Li_{3+x}La_3M_2O_{12}$ at RT.[11] Reproduced with permission.[11] Copyright (2012), American Physical Society.

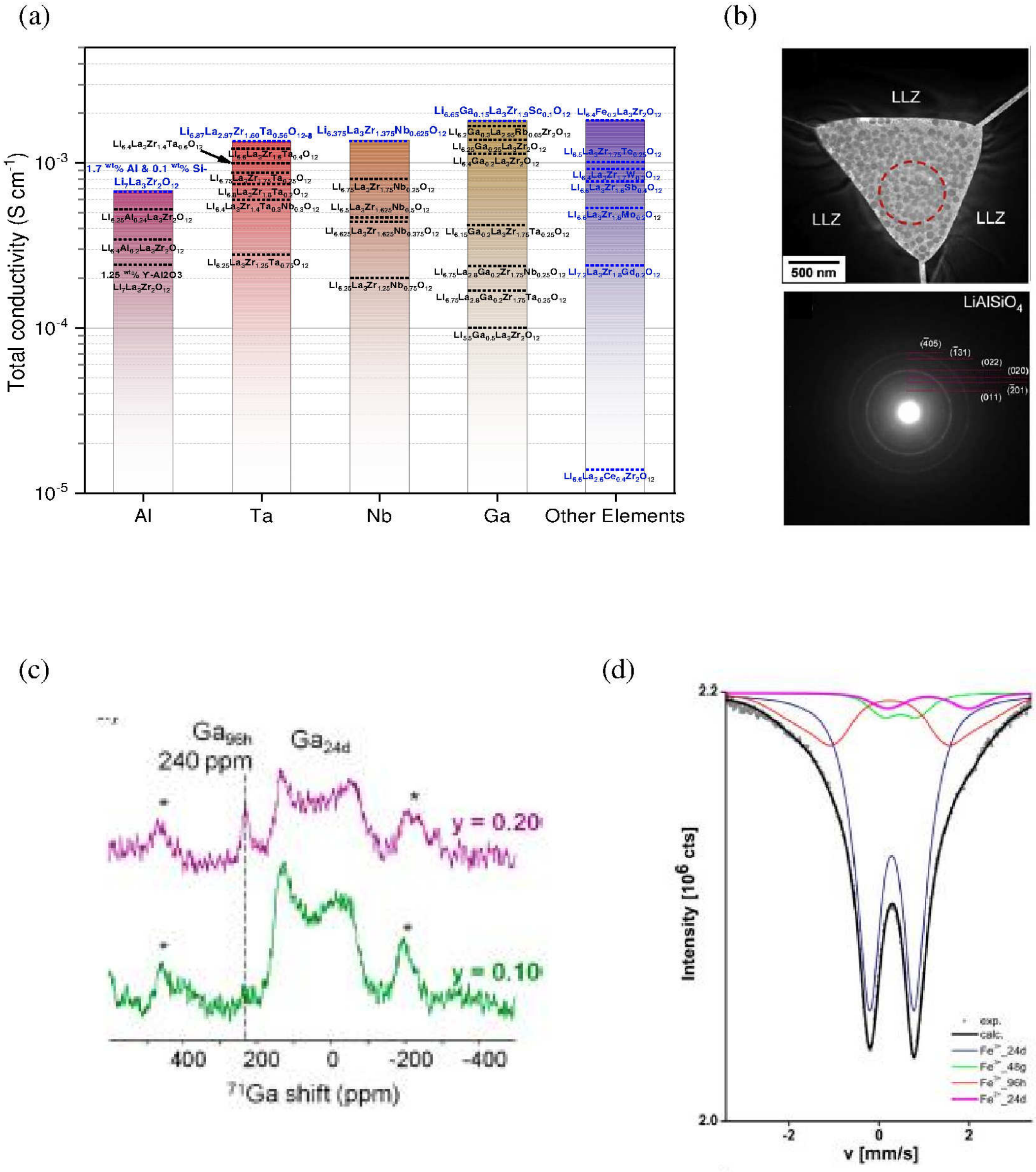

Figure 2. Development of LLZO based solid electrolyte. **(a)** Total conductivity of LLZO with different substitutions. **(b)** TEM image (top) and selected area electron diffraction pattern (bottom) of LLZO around a triple-point grain boundary.[13] $LiAlSiO_4$ is acuminated at grain boundary. Reproduced with permission.[13] Copyright 2011, Elsevier. **(c)** Solid state ^{71}Ga NMR spectra of $Li_{6.55+y}Ga_{0.15}La_3Zr_{2-y}Sc_yO_{12}$ to show Ga^{3+} has preference to *24d* Li(1) sites.[15] Reproduced with permission.[15] Copyright 2017, American Chemical Society. **(d)** Mössbauer spectra show Fe-ions of $Li_{7-3x}Fe_xLa_3Zr_2O_{12}$ at 295 K have preference to *24d* Li(1) sites.[21] Reproduced with permission.[21] Copyright 2013, American Chemical Society.

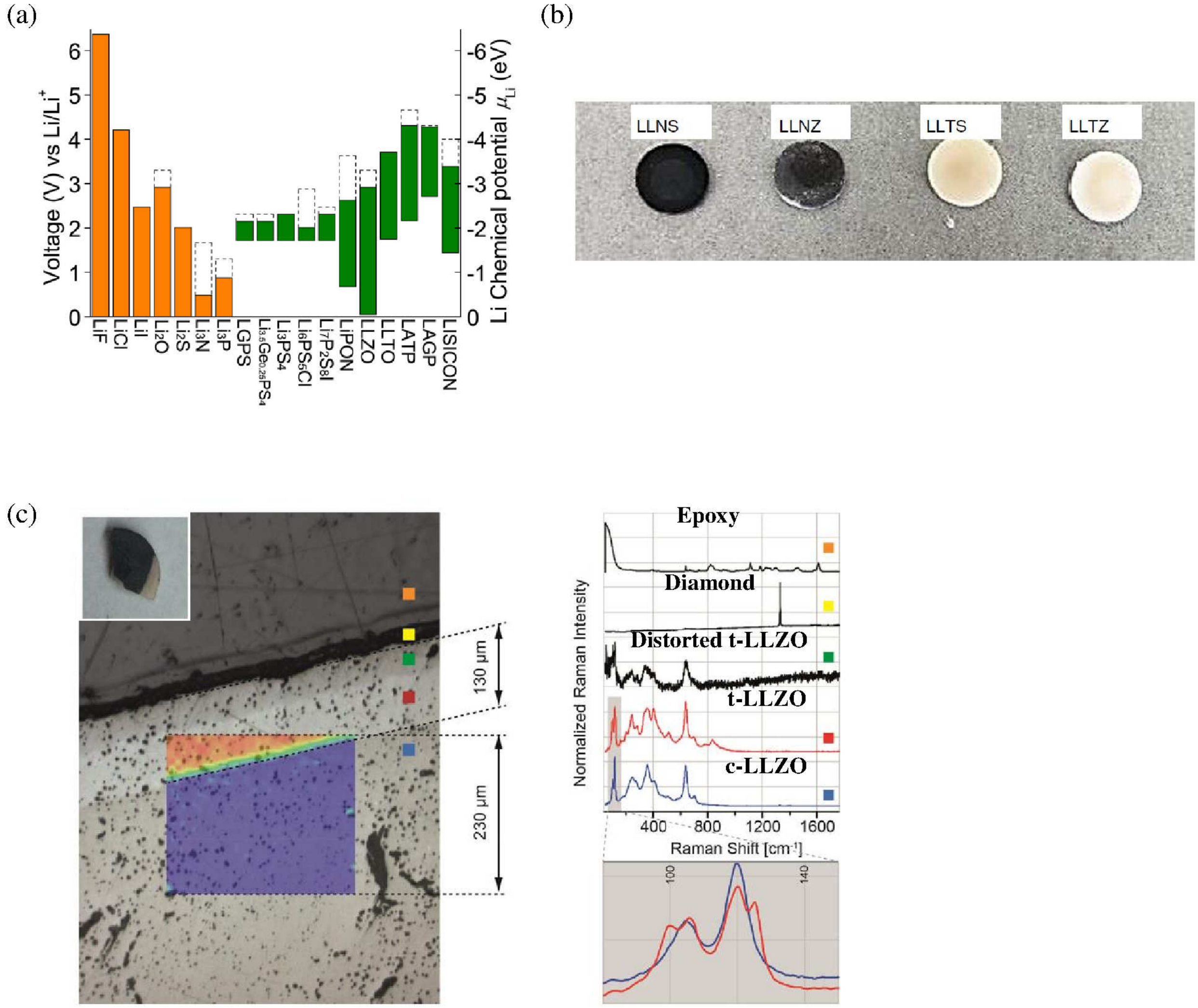

Figure 3. LLZO chemical stability toward metallic Li. **(a)** First principle calculated electrochemical window (solid color bar) of solid electrolyte and other materials. The oxidation potential to fully delithiate the material is marked by the dashed line.[63] Reproduced with permission.[63] Copyright 2015, American Chemical Society. **(b)** A photograph to show that the interface of Nb-substituted LLZO were reduced by Li metal (black color) after in contact for 60 days while Ta-substituted LLZO stayed the same color.[43] Reproduced with permission.[43] Copyright 2015, Elsevier. **(c)** Raman mapping of the $Li_{6.4}Fe_{0.2}La_3Zr_2O_{12}$; the picture (left) shows a cross section after the solid electrolyte has been in contact with metallic Li, spectra for different areas of the cross section (top right) and magnification of the shaded area in spectra. [22] Reproduced with permission.[22] Copyright 2018, American Chemical Society.

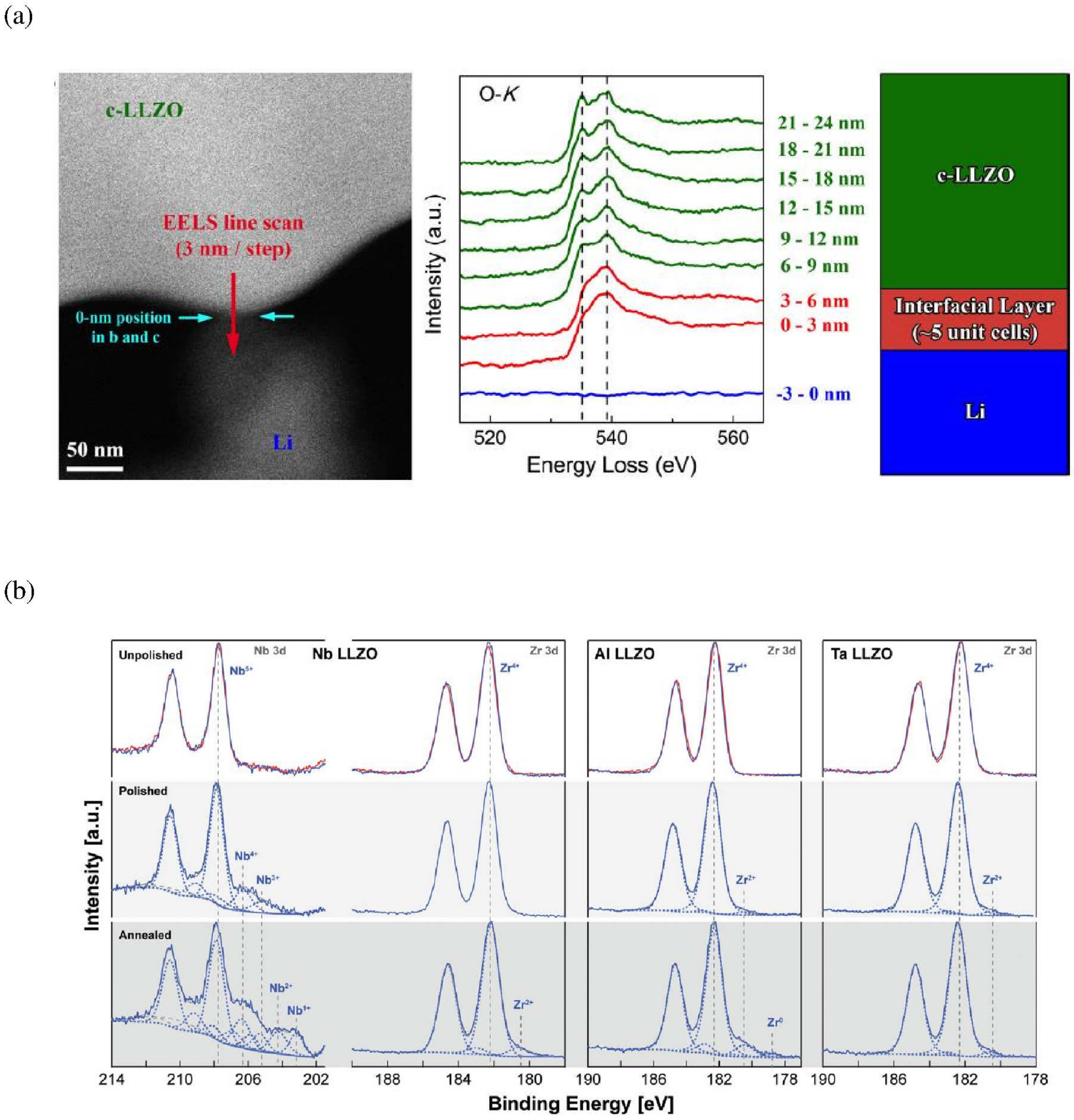

Figure 4. LLZO chemical stability toward metallic Li. **(a)** HAADF-STEM image of c-LLZO in situ contacted with Li (left). The O K-edges obtained in the EELS line scan (middle). Schematic illustration of the interfacial behavior suggested by the EELS line scan (right).[64] Reproduced with permission.[64] Copyright 2016, American Chemical Society. **(b)** Nb 3d and Zr 3d core level XPS spectra from Nb-, Al-, and Ta-doped LLZO with unpolished (top), polished (middle) and UHV heated (bottom) surfaces before (red) and after (blue) Li deposition.[65] Reproduced with permission.[65] Copyright 2019, Wiley-VCH.

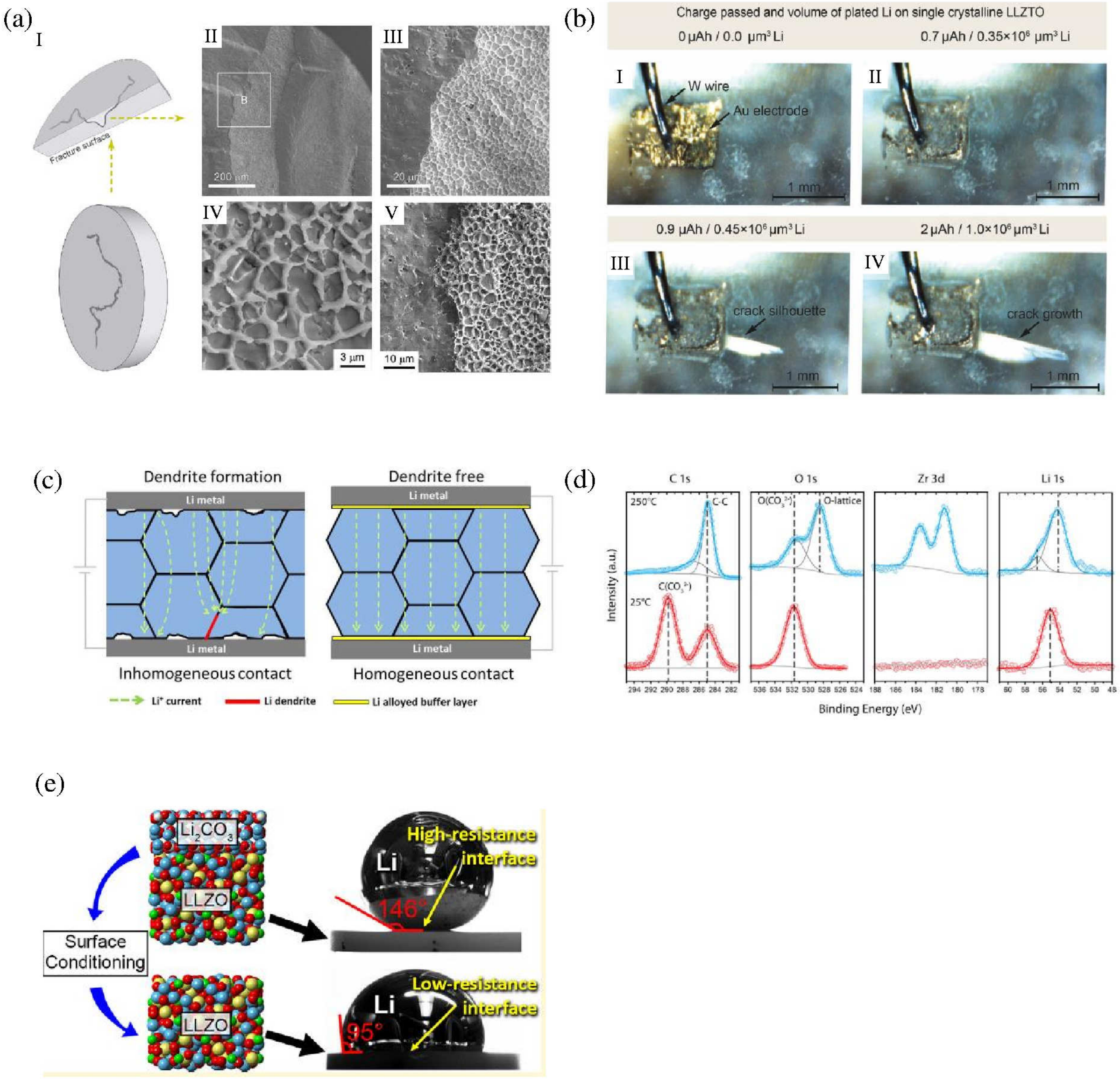

Figure 5. The development of negative electrode for CLBs. **(a)** SEM Li dendrite structure in cycled LLZO (I) illustration of a fractured surface due to Li dendrite, (II) SEM image of a fracture surface, (III) enlarged SEM micrograph of the boxed area B in (II), (IV) higher magnification SEM image of the web structure in (III), and (V) SEM images of the web structure after exposure to air.[69] Reproduced with permission.[69] Copyright 2017, Elsevier. **(b)** Optical microscopy images of a polished single crystal of LLZTO. The white silhouette is the propagate crack that created by Li dendrite.[72] Reproduced with permission.[72] Copyright 2017, Wiley-VCH. **(c)** illustration of Li dendrite formation due to inhomogeneous contact between LLZO and Li electrode that can be solved by a Au interlayer coating.[39] Reproduced with permission.[39] Copyright 2016, American Chemical Society. **(d)** XPS scan of C 1s, O 1s, Zr 3d, and Li 1s spectra collected in 200 mTorr of Ar at RT: 25 °C (bottom) and 250 °C (top). The C(CO3) peak at 290 eV completely disappeared indicates Li_2CO_3 can be remove from LLZO surface by heating up to 250 °C.[75] Reproduced with permission.[75] Copyright 2018, American Chemical Society. **(e)** Contact angle between LLZO and molten Li with Li_2CO_3 (top) and without Li_2CO_3 by fine polishing and heat treatment at 500 °C (bottom).[71] Reproduced with permission.[71] Copyright 2017, American Chemical Society.

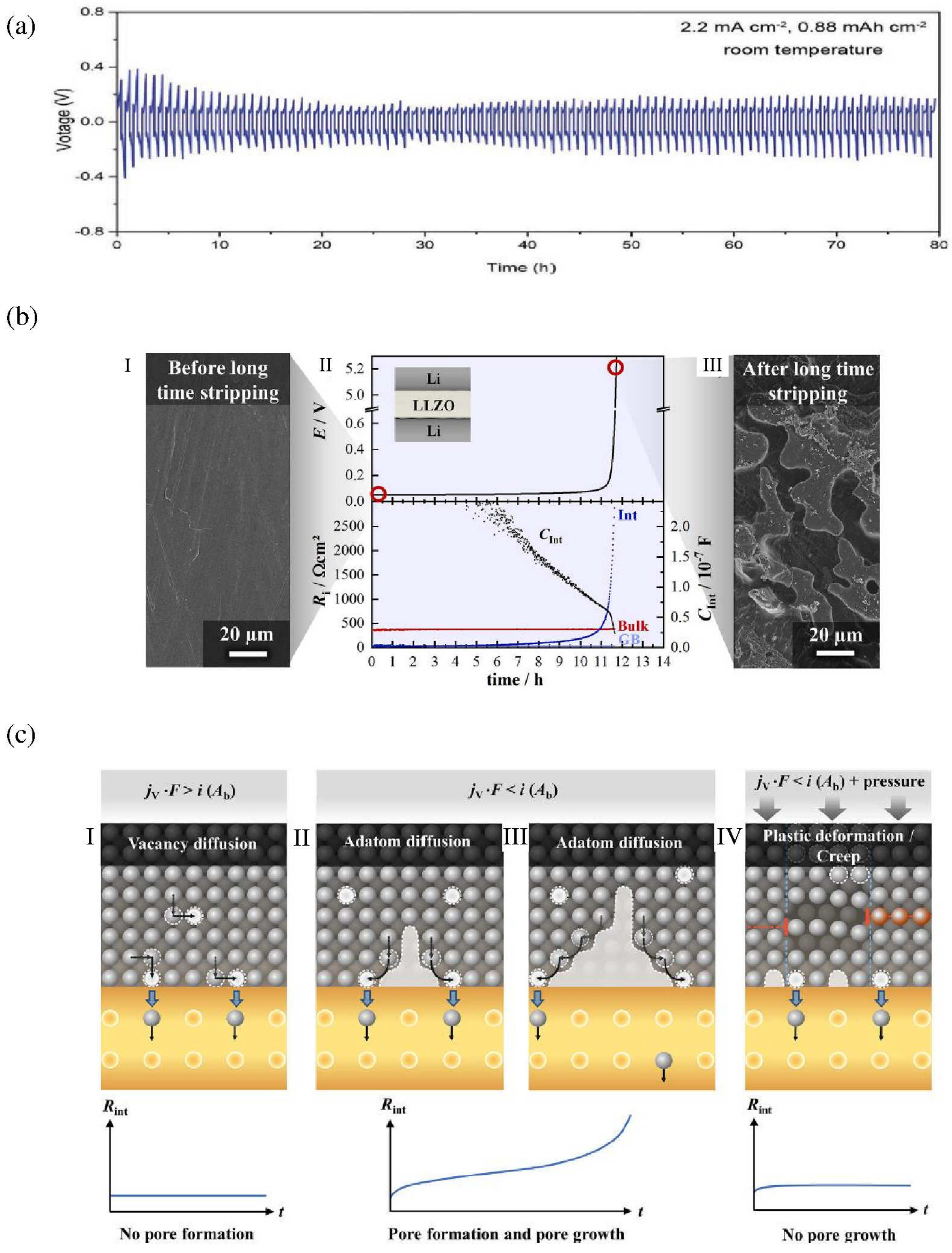

Figure 6. The development of negative electrode for CLBs. **(a)** Galvanostatic cycling of Li/LLZO/Li at 2.2 mA·cm^{-2} for 0.88 mA h·cm^{-2} for 100 cycles.[77] Reproduced with permission.[77] Copyright 2019, Wiley-VCH. **(b)** Morphology of the lithium metal electrode before assembling the symmetric cell (I) and after stripping at 100 µA·cm^{-2} anodic load (III). The potential profile and impedance contributions shows a complete contact loss of Li electrode after around 12 h of stripping (II). **(c)** Schematic of the different mechanisms that facilitate charge transfer at the lithium metal electrode under anodic load (limiting cases).[98] (I) local current density does not exceed the vacancy diffusion limit. (II, III) local current density exceeds the diffusion limit (IV) external pressure is applied.[98] Reproduced with permission.[98] Copyright 2019, American Chemical Society.

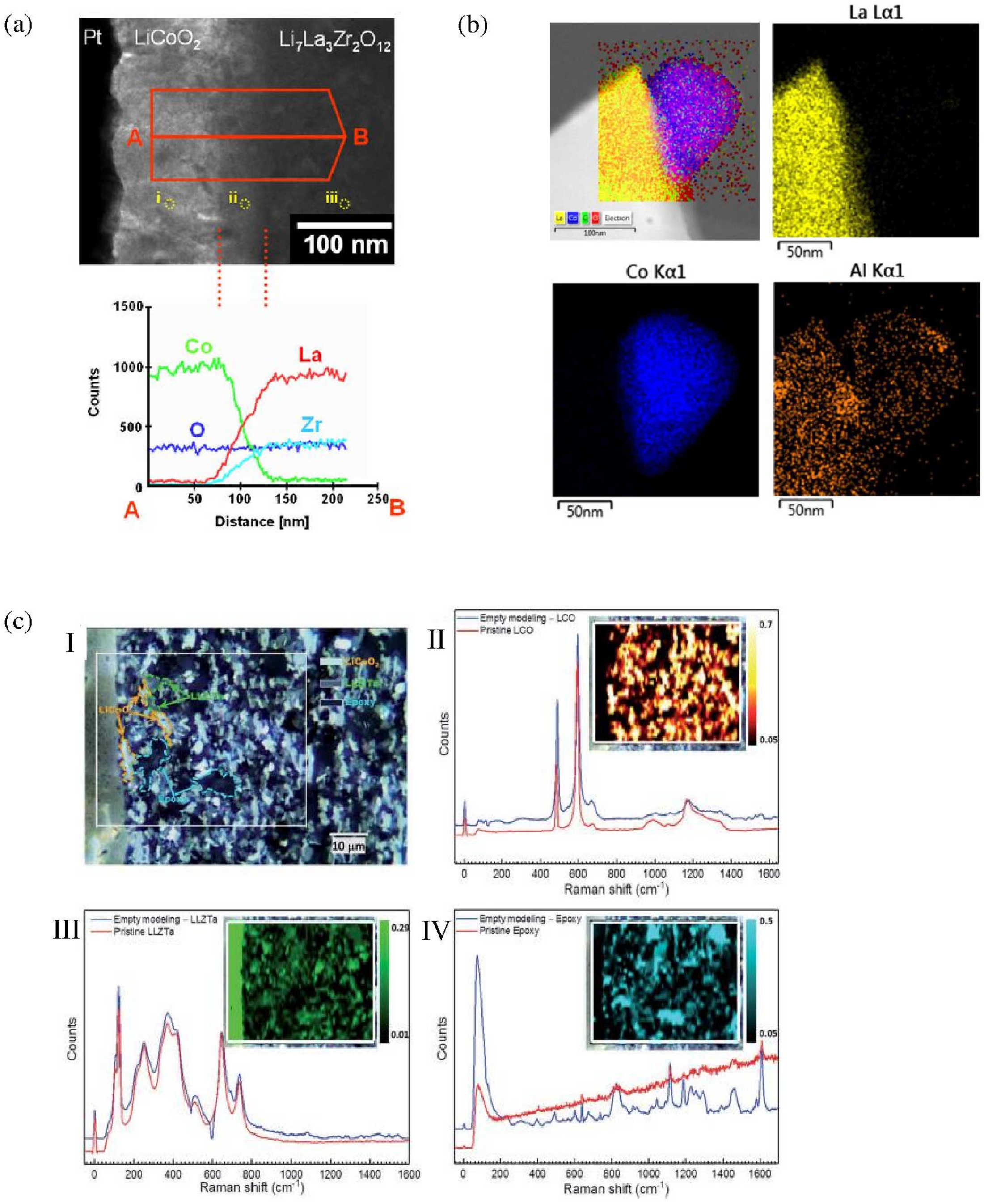

Figure 7. The development of positive electrode for CLBs. (a) Cross-sectional TEM image of an LLZ/ PLD deposited LCO thin film interface (top) and the EDS line profile (bottom).[103] Reproduced with permission.[103] Copyright 2011, Elsevier. **(b)** TEM images of crystalline LCO/LLZO that was directly obtained from LCOon a LLZO pellet and the corresponding EDS elemental mappings to show Al^{3+} diffused into LCO after heat treated at 700 °C.[102] Reproduced with permission.[102] Copyright 2013, American Chemical Society. **(c)** High-resolution micro-Raman mapping of a CLB cross-section which was sintered at 1050 °C in air. (I) Optical image of the SSLB cross-section and its mapping area. The Raman mappings and the spectra for (II) LCO, (III) LLZ:Ta and (IV) epoxy.[105] Reproduced with permission.[105] Copyright 2019, Royal Society of Chemistry.

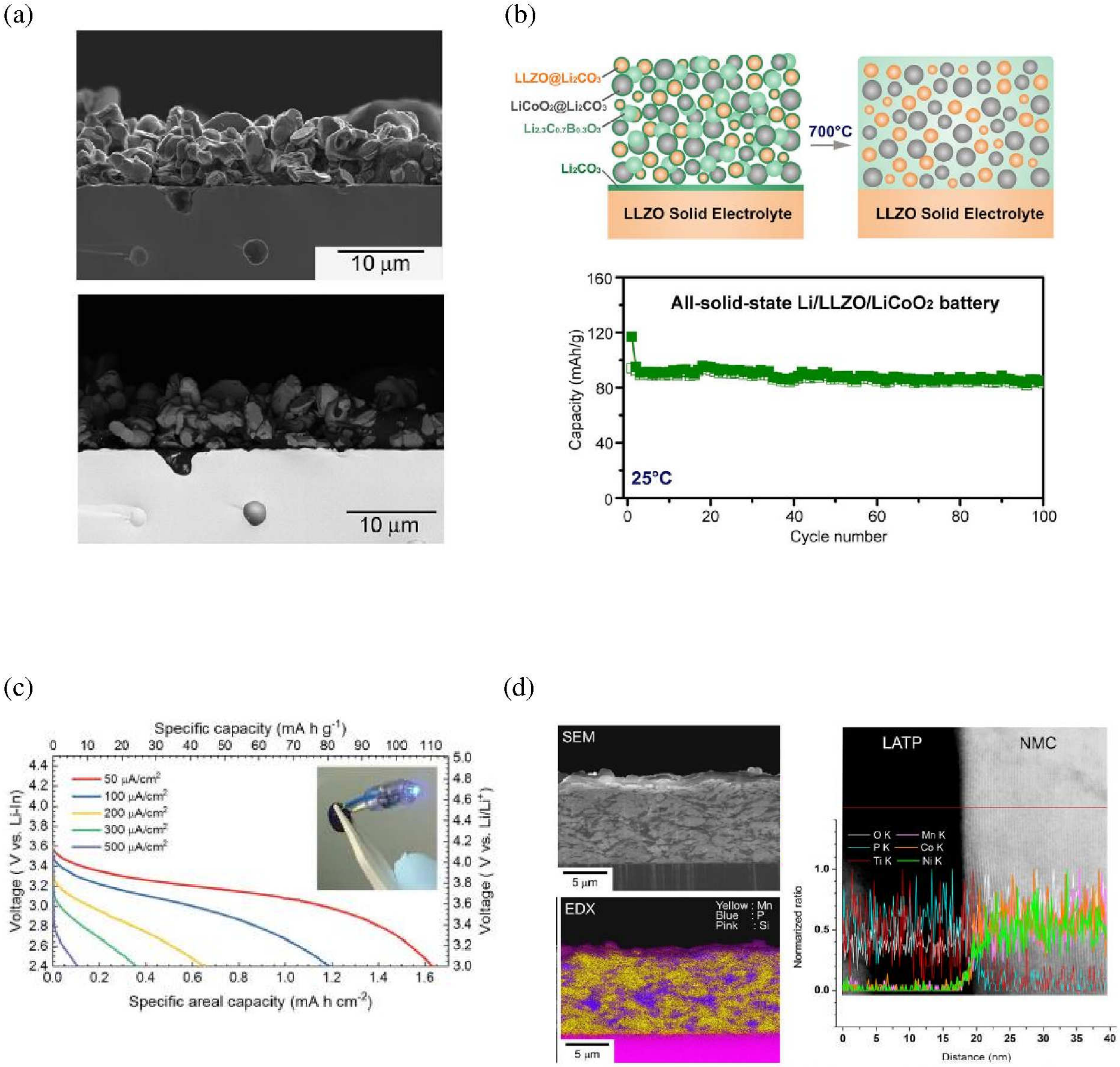

Figure 8. The development of positive electrode for CLBs. **(a)** Cross-sectional SEM images of secondary electron (top) and backscattering electron (bottom) images of the interface between the positive electrode layer (LCO positive active electrode material and Li_3BO_3 solid electrolyte) and the $Li_{6.75}La_3Zr_{1.75}Nb_{0.25}O_{12}$ solid electrolyte.[112] Reproduced with permission.[112] Copyright 2013, Elsevier. **(b)** Thermally soldering LCO and LLZO through the reaction between the $Li_{2.3}C_{0.7}B_{0.3}O_3$ and the Li_2CO_3 that can be spontaneously coated $Li_{2.3-x}C_{0.7+x}B_{0.3-x}O_3$ interphase on both LLZO and LCO. The CLB with such a CPE exhibits high cycling stability and high rate performance.[110] Reproduced with permission.[110] Copyright 2018, Cell.

(c) CLB using LCO/LLZTaO as CPE allows high discharge current densities and capacities.[105] Reproduced with permission.[105] Copyright 2019, Royal Society of Chemistry. **(d)** Cross-sectional SEM images and EDX mapping of a $LiNi_{1/3}Co_{1/3}Mn_{1/3}O_2$ (NMC)-LATP composite film on Si/SiO_2 wafer by aerosol deposition (left). TEM image of a NMC/LATP interface in the NMC-LATP composite film and its EDX line profiles to show no interface reaction between NMC and LATP during aerosol deposition.[117] Reproduced with permission.[117] Copyright 2016, Elsevier.